J. Fluid Mech. (1993), *vol.* 250, *pp.* 69–101

Measurements of the primary instabilities of film flows

By JUN LIU, JONATHAN D. PAUL AND J. P. GOLLUB

Department of Physics, Haverford College, Haverford, PA 19041, USA
and Department of Physics, University of Pennsylvania, Philadelphia, PA 19104, USA

(Received 17 July 1992 and in revised form 3 November 1992)

We present novel measurements of the primary instabilities of thin liquid films flowing down an incline. A fluorescence imaging method allows accurate measurements of film thickness $h(x, y, t)$ in real time with a sensitivity of several microns, and laser beam deflection yields local measurements with a sensitivity of less than one micron. We locate the instability with good accuracy despite the fact that it occurs (asymptotically) at zero wavenumber, and determine the critical Reynolds number R_c for the onset of waves as a function of angle β. The measurements of $R_c(\beta)$ are found to be in good agreement with calculations, as are the growth rates and wave velocities. We show experimentally that the initial instability is convective and that the waves are noise-sustained. This means that the waveform and its amplitude are strongly affected by external noise at the source. We investigate the role of noise by varying the level of periodic external forcing. The nonlinear evolution of the waves depends strongly on the initial wavenumber (or the frequency f). A new phase boundary $f_s^*(R)$ is measured, which separates the regimes of saturated finite amplitude waves (at high f) from multipeaked solitary waves (at low f). This boundary probably corresponds approximately to the sign reversal of the third Landau coefficient in weakly nonlinear theory. Finally, we show that periodic waves are unstable over a wide frequency band with respect to a convective subharmonic instability. This instability leads to disordered two-dimensional waves.

1. Introduction

Thin liquid films flowing down an incline are found frequently in engineering and natural processes. Flowing films are unstable when their Reynolds numbers are larger than a critical value R_c. The resulting interfacial waves show fascinating nonlinear phenomena (Kapitza & Kapitza 1949; Fulford 1964; Dukler 1972; Sivashinsky & Michelson 1980; Alekseenko, Nakoryakov & Pokusaev 1985; Lin & Wang 1985; Kelly *et al.* 1989; Goussis & Kelly 1991; Lacy, Sheintuch & Dukler 1991; Liu *et al.* 1992), including solitary waves with one or more peaks, transverse secondary instabilities, and complex disordered patterns. Despite the rather voluminous literature on this problem, several basic questions have not been adequately settled experimentally. First, does the dependence of the critical Reynolds number on the angle of inclination agree with the predictions of stability theory? This simple question is not an easy one to answer because the instability occurs at zero wavenumber where it is hard to observe. Second, is the primary instability convective or absolute? This question is quite important, since it bears on the extent to which the resulting macroscopic waves are influenced by microscopic noise near the source. Third, how is the nonlinear development of periodic waves affected by their frequency? It is known that the isolated solitary waves found

at low frequency are quite different from the saturated, more nearly sinusoidal waves found at high frequency, but the question of the existence of a definite phase boundary separating these two regimes has not been addressed experimentally. Finally, what are the basic mechanisms leading to spatially disordered film flows?

The purpose of this paper is to answer these questions using experimental methods somewhat more sophisticated than those used previously, including a fluorescence imaging technique that allows the film thickness $h(x, y, t)$ to be determined directly, and a sensitive probe for wave slopes that can resolve waves when they are as small as a few microns in amplitude. These methods, along with the relatively small Reynolds number and the relatively well developed state of the theory, make the film flow system attractive to study. The paper is organized as follows. In §2, we discuss the extensive literature relevant to this investigation. The novel experimental methods are described in §3. The experimental results are presented in §4 and summarized in §5.

2. Background

2.1. *Geometry and parameters*

The system of interest (in its simplest form) is an incompressible Newtonian fluid flowing down an inclined plane that makes an angle β with the horizontal. Coordinates are usually chosen such that x is the downstream direction, y is the transverse coordinate in the film plane, and z is perpendicular to the film plane (x, y). The important parameters are: (*a*) the Reynolds number $R = h_0 u_0/\nu$, based on the unperturbed film thickness h_0, the fluid velocity u_0 at the surface, and the kinematic viscosity ν; and (*b*) the Weber number $W = \gamma/(\rho h_0^2 g \sin\beta)$, where γ is the surface tension, ρ the density of the fluid, and g the gravitational acceleration. The Weber number W is not independent of the Reynolds number R, so a dimensionless parameter $N_\gamma = \gamma(2/\rho^3\nu^4 g)^{\frac{1}{3}}$ is sometimes used to represent the effect of surface tension. The surface velocity of the stationary primary flow is $u_0 = g h_0^2 \sin\beta/(2\nu)$. The velocity field is designated as (u, v, w) and the film thickness $h(x, y, t)$. Dimensionless quantities are used unless otherwise specified. The lengthscale is set as h_0, the velocity scale is u_0, and the timescale is h_0/u_0. Various assumptions that may be more or less valid for experiments are often (but not always) made: that the fluid is isothermal; that the system is laterally infinite in the y-direction; that there is no air flow over the film; and that the fluid surface is uncontaminated.

2.2. *Linear stability theory*

We summarize the linear stability theory of film flows, which has still not been fully tested. The theory is based on analysis of the Orr–Sommerfeld equation with appropriate boundary conditions (Yih 1955, 1963; Benjamin 1957) which are derived by linearizing the Navier–Stokes equations with the assumption of two-dimensional infinitesimal disturbances. For simplicity, the origin of coordinates is located at the surface of the unperturbed film and the positive z-axis is directed downward. With these choices, the unperturbed film surface is $z = 0$ and liquid–solid boundary is at $z = 1$. The dimensionless velocity profile of the stationary primary flow is a parabolic function:

$$u = 1 - z^2. \tag{1}$$

The disturbance is represented by

$$\eta = \delta \exp[\mathrm{i}(\alpha x - \omega t)], \tag{2}$$

where δ is the initial perturbation amplitude, $\alpha = 2\pi h_0/\lambda$ is the dimensionless

wavenumber and $\omega = 2\pi f h_0/u_0$ is the dimensionless angular frequency, where f is the wave frequency. The analysis is termed 'spatial' or 'temporal' depending on whether α or ω is allowed to be complex. Both methods give the same critical conditions for the onset of the instability. The Orr–Sommerfeld equation can be written as follows:

$$\phi_{zzzz} - 2\alpha^2\phi_{zz} + \alpha^4\phi = \mathrm{i}\alpha R[(U-\omega/\alpha)(\phi_{zz} - \alpha^2\phi) - U_{zz}\phi], \tag{3}$$

where ϕ is the dimensionless stream function for the velocity perturbation, the index z indicates differentiation with respect to z, and U is the dimensionless velocity of the primary flow and is usually taken as equation (1). The equations cannot be solved analytically. Benjamin (1957) and Yih (1963) first performed approximate analytical calculations for the cases of long waves and small Reynolds numbers. Approximate analytical solutions not restricted to small R were developed by Anshus & Goren (1966) and Krantz & Goren (1971*a*). Numerical solutions were given by Whitaker (1964), Pierson & Whitaker (1977) and Chin, Abernathy & Bertschy (1986).

The instability occurs for sufficiently long waves $\alpha < \alpha_c(R)$ when the Reynolds number is above its critical value R_c. The upper cutoff wavenumber α_c is determined by surface tension, which damps the short wavelengths. The critical Reynolds number for the onset of instability is expected to be

$$R_c = \tfrac{5}{4}\cot\beta, \tag{4}$$

though this prediction has not yet been tested quantitatively. The unstable region is bounded by two neutral curves in the α *vs.* R plane when $R > R_c$. The lower one is the line $\alpha = 0$, and the upper one is $\alpha_c(R)$. The growth rate and phase velocity of waves with infinitesimal amplitudes can be calculated numerically as functions of wavenumber for fixed R, W and β. For infinitesimal wavenumber, the phase speed (c) is twice the surface fluid velocity of the unperturbed film, i.e. $c = 2$.

In this paper we apply an approximate method of solution due to Anshus & Goren (1966) to solve the Orr–Sommerfeld equation (3) for comparison with experiments. Their method is based on replacing $U = 1 - z^2$ in (3) by $U = 1$, but its second spatial derivative is set equal to -2 in other terms. Anshus & Goren showed that their method is quite accurate for large surface tension parameter $N_\gamma (> 10)$ and moderate $R (< 200)$. We have also checked the approximate solutions by comparison with numerical computations (Pierson & Whitaker 1977) for a vertical water film with $1 \leqslant R \leqslant 1000$.

2.3. *Convective character of the instability*

Elucidation of the concepts of convective and absolute instabilities (Deissler 1987*a*, 1989; Huerre & Monkewitz 1990) has stimulated the study of open flow systems from a new perspective (Babcock, Ahlers & Cannell 1991; Schatz, Tagg & Swinney 1991; Steinberg & Tsameret 1991; Babcock, Cannell & Ahlers 1992). In convectively unstable systems, a perturbation grows with respect to coordinates moving with the disturbance, but decays in the laboratory frame of reference because the structures are carried downstream. On the other hand, an absolutely unstable system manifests growth of small perturbations at a fixed laboratory coordinate. Any system with non-zero group velocity will be convectively unstable sufficiently close to the onset of instability (Deissler 1989). Some open flow systems, such as wakes, capillary jets and Taylor–Couette flow with through-flow, are known to show both convective and absolute instabilities, depending on flow conditions (Huerre & Monkewitz 1990; Babcock *et al.* 1991). Some open systems, for example two-dimensional plane Poiseuille flow (Deissler 1987*b*), show only convective instability.

The important consequence of this distinction is that a convective instability is

extremely sensitive to external noise near the source. The resulting macroscopic patterns are in fact 'noise-sustained structures' whose amplitudes can depend on the amount of external noise (Deissler, 1987*a*, 1989). On the other hand, patterns resulting from an absolute instability are much less sensitive to external noise, except during their initiation. In physical systems the sources of noise, which can never be completely eliminated, include small mechanical vibrations and thermal fluctuations. Even microscopic noise may contribute to macroscopic structure in convectively unstable systems (Babcock *et al.* 1992; Deissler & To 1992). The nature of chaotic states that can result from convective and absolute instabilities is also significantly different (Deissler 1987*a*, 1989).

Benjamin (1961) first noted the convective character of the instability of film flows. He showed both theoretically and experimentally that a localized linear disturbance is transported downstream. However, the properties of the convective instability were not studied quantitatively.

We have used a long-wave expansion equation due to Benney (1966) to study the nature of the film flow instability near its onset because the full dispersion relation $\omega(\alpha)$ from the Orr–Sommerfeld equation and its boundary conditions cannot be treated analytically. For two-dimensional disturbances with wavelength much longer than the average film thickness ($\lambda \gg h_0$), the dimensionless evolution equation is

$$h_t + 2h^2 h_x + \tfrac{2}{3}[\tfrac{4}{5}Rh^6 h_x - h^3 h_x \cot\beta + Wh^3 h_{xxx}]_x = 0 \tag{5}$$

to the first order in α, where indices x and t denote partial derivatives. It should be pointed out that the surface tension term $(Wh^3 h_{xxx})_x$ is actually of order α^3, but it is kept because, near R_c, $W\alpha^2 \sim O(1)$ (Gjevik 1970). Equation (5) is valid for Reynolds numbers sufficiently close to R_c when the surface tension is non-zero. As a nonlinear evolution equation, it is expected to be valid only for $R \sim O(1)$. It is straightforward to do a linear stability analysis of (5) by following the methods discussed by Huerre & Monkewitz (1990). Our calculations (Liu *et al.* 1992) show that the system becomes convectively unstable at R_c given by (4) if the surface tension is non-zero.

The analysis also predicts a convective–absolute instability transition at $R_{c/a} \approx R_c + (6.70W)^{\frac{1}{3}}$. However, careful examination of the conditions of validity of (5) reveals that $R_{c/a}$ is sufficiently high that the dominant wavenumbers are too large to be within the domain of validity of the long-wave expansion. We therefore concluded that the question of the existence of a convective–absolute transition cannot be settled within the framework of the long-wave approximation. An analysis of the full hydrodynamic equations may be required. Joo & Davis (1992*a*) independently did similar calculations for the case of film flows on a vertical plane by using a long-wave expansion equation related to (5). Previously, Deissler, Oron & Lee (1991) found a convective–absolute transition for a modified Kurmamoto–Sivashinsky equation intended as a model of film flows on a vertical cylindrical surface.

2.4. *Nonlinear stability theory*

Nonlinear evolution equations which are much simpler than the full Navier–Stokes equations are often used to study the nonlinear behaviour of film flows. These are derived under the assumption that the wavelength is sufficiently large ($\epsilon = h_0/\lambda \ll 1$). Two somewhat different approaches have been used: a long-wave expansion approximation for low Reynolds number $R \sim O(1)$ (Benney 1966; Gjevik 1970, 1971; Roskes 1970; Lin 1974); and an 'integral boundary-layer approximation' that is valid at somewhat larger Reynolds numbers $R \sim O(\epsilon^{-1})$ (Kapitza 1948; Shkadov 1967; Lee 1969; Alekseenko *et al.* 1985; Prokopiou, Cheng & Chang 1991). Equation (5) is a long-

wave expansion equation. The ranges of validity of these approximate theories have not been checked experimentally.

Weakly nonlinear analysis shows that the evolution of the two-dimensional waves depends strongly on the initial wavenumber (Lin 1969, 1974; Gjevik 1970; Agrawal & Lin 1975; Nakaya 1975). There exists a wavenumber $\alpha_s(R)$, which is determined by the sign reversal of the cubic term in the Landau equation for the wave amplitude, such that when $\alpha_s(R) < \alpha(R) < \alpha_c(R)$, especially for α close to α_c, an unstable infinitesimal wave may evolve into a supercritically stable, small finite-amplitude wave. On the other hand, when $\alpha(R) < \alpha_s(R)$, strong nonlinearity promotes further evolution because the first several harmonics lie in the unstable region predicted by the linear theory; modal interactions are strong and saturation does not occur. However, weakly nonlinear theory cannot predict the evolution of waves in this range. Based on the analysis of (5) (Gjevik (1970) obtained an approximate expression for the boundary $\alpha_s(R)$:

$$\alpha_s = \tfrac{1}{2}\alpha_c = [(1/5W)(R-R_c)]^{\frac{1}{2}}. \tag{6}$$

Since the fastest-growing wavenumber predicted by the linear analysis of (5) is $\alpha_m = \alpha_c/\sqrt{2}$, we have $\alpha_m > \alpha_s$. Lin (1969, 1974) and Nakaya (1975) gave similar but more complicated results. Numerical simulations by Joo, Davis & Bankoff (1991) based on a Benney-type long-wave expansion agree qualitatively with these predictions. However, they pointed out that the actual α_s obtained through numerical simulations would necessarily be larger than α_m except near R_c.

Into what kinds of structures do the low-wavenumber small-amplitude waves evolve? Kapitza & Kapitza (1949) noted the existence of stationary 'single' (or solitary) waves which (after further evolution) develop subsidiary peaks in front. Pumir, Manneville & Pomeau (1983) demonstrated that large-amplitude solitary waves are described by homoclinic trajectories in a phase space spanned by the film thickness and its derivatives. Several kinds of degenerate solitary waves may exist, characterized by different numbers of maxima. This was confirmed later by Nakaya (1989) with a different approach. Tsvelodub (1980) and Joo *et al.* (1991) performed numerical simulations of Benney-type long-wave expansion equations, and found solitary-wave solutions for small wavenumbers. Using the integral boundary-layer approximation, Trifonov & Tsvelodub (1991) and Trifonov (1992) obtained steady travelling periodic waves for vertical flowing films. In some but not all cases, the calculated wave profiles were in good agreement with previous experimental results. Recently, Chang, Demekhin & Kopelevich (1993) developed a new long-wave boundary-layer approximation and compared its predictions with experiments.

Chang and collaborators (Chang 1989; Prokopiou *et al.* 1991) applied bifurcation techniques to study a third-order long-wave expansion equation for $R \sim O(1)$ and a second-order (in $\epsilon = h_0/\lambda$) integral boundary-layer approximation equation intended to describe the nonlinear behaviour at intermediate $R \sim O(\epsilon^{-1})$. Near the critical point, they found several novel families of solutions. When $\alpha \to 0$, homoclinic orbits are found that correspond to solitary waves. However, when $\alpha \to \alpha_c$, supercritical limit cycles occur; these correspond to sinusoidal travelling waves. Their analysis implies the existence of a boundary $\alpha_s(R)\,(0 < \alpha_s(R) < \alpha_c(R))$ separating these two regions which bifurcate differently from the stationary state.

To elucidate the transitions to disordered waves, one must understand the instability of nonlinear periodic waves, which is due in part to a spatial subharmonic instability. The subharmonic instability of film flows has been analysed by several researchers. Prokopiou *et al.* (1991) showed that there exists a band of periodic waves near the upper neutral curve $\alpha_c(R)$ that are unstable to subharmonic instability. Joo & Davis

(1992*b*) also demonstrated the existence of spatial subharmonic instability by means of numerical simulations of (5). In a more general treatment of subharmonic instabilities, Cheng & Chang (1992) concluded that a finite-amplitude wave is always unstable to disturbances with half its wavenumber (or frequency) if the subharmonic is also linearly unstable. This is the case for film flows on an inclined plane, where all wavenumbers smaller than $\alpha_c(R)$ are linearly unstable.

2.5. *Previous experiments*

A few experiments have been compared quantitatively with linear theories (Krantz & Goren 1971*a*; Pierson & Whitaker 1977; Alekseenko *et al.* 1985; Lin & Wang 1985). The wave velocity and wavelength have been determined for small-amplitude natural waves, and compared with the fastest growing disturbance in linear theory. These data lead to semi-quantitative agreement with theoretical predictions but with fairly large scatter. The spatial growth rate and phase velocity were measured as functions of wavenumber by Krantz & Goren (1971*a*) for oil films at $R < 2$ and $\beta = 74.5°$ and 90°. The results agree quite well with linear theory (Krantz & Owens 1973).

A parabolic velocity profile is often assumed in formulating linear and nonlinear stability theories. Bertschy, Chin & Abernathy (1983) found that the velocity profile of primary flow is nearly parabolic even at $R \sim 2000$. Alekseenko *et al.* (1985) measured the instantaneous velocity field in a wavy liquid film and showed that a self-similar parabolic velocity profile is more appropriate.

Surprisingly, the critical Reynolds number $R_c(\beta)$ as a function of inclination angle has not been measured adequately. The available results have been collected by Fulford (1964), but much of the data were based on visual observation rather than quantitative measurement. The results generally lie quite far above the prediction of (4). As we explain later, the fact that the instability occurs at $\alpha = 0$ makes careful measurement essential for determining the stability boundary. A referee pointed out to us that Koehler (Koehler 1968) also made some measurements of R_c in his unpublished dissertation.

Abundant observations have been made of nonlinear phenomena including solitary waves, the evolution of subsidiary wavefronts, the development of three-dimensional instabilities, and the production of irregular fully developed waves (Kapitza & Kapitza 1949; Tailby & Portalski 1962; Krantz & Goren 1971*b*; Chu & Dukler 1974, 1975; Brauner & Maron 1982; Alekseenko *et al.* 1985; Lacy *et al.* 1991). Experiments have shown the strong dependence of the nonlinear evolution of wavy films on initial wavenumber. The existence of saturated waves has also been demonstrated by Krantz & Goren (1970). However, the phase boundary $\alpha_s(R)$ predicted by nonlinear theory appears not to have been measured experimentally. Brauner & Maron (1982) studied the spatial evolution of the power spectrum of natural waves experimentally, and concluded that there is a frequency reduction process. Their results suggest that subharmonic instability may be involved. Because the natural waves are always irregular, Kapitza & Kapitza (1949), Krantz & Goren (1971*a*), and Alekseenko *et al.* (1985) introduced sinusoidal perturbations at the film entrance to regulate the waves. This allowed them to study both linear and nonlinear waves at specific frequencies.

The previous experiments, though extensive, have been based mainly on local probes and photography. Computer-based imaging methods have apparently not been previously applied to the nonlinear development of film flows.

3. Experimental methods

In this section we first describe the system for producing and perturbing the film flows, which is computer controlled but otherwise not particularly original. We then describe the local probes of wave slope, and the analysis used to interpret the data on wave growth. These probes are especially sensitive, and allow exploration of the noise sensitivity that is the characteristic of convective instabilities. Finally, we discuss the fluorescence imaging system, which we use to obtain quantitative measurements of the film thickness as a function of space and time.

3.1. *Flow and perturbation system*

The flow and measurement systems are shown schematically in figure 1. The fluid is pumped through filters to limit contamination and through a ballast tank to prevent pump vibrations from reaching the film. It emerges from an input manifold through a narrow but adjustable gap between the film plane and an overlying plate. The dimensions of the film plane are 200 cm parallel to the flow by 50 cm transverse to the flow. The supporting framework of the film plane is massive and mounted on rubber feet to reduce the influence of any building vibrations. The input manifold contains a copper mesh as a precaution against fluid oscillations inside the manifold. The system can accommodate fluids with a range of viscosities from 1×10^{-6}–10×10^{-6} m^2/s. The angle β can be continuously adjusted over the range 0–35°. This allows the phase velocity and the amplification rate of waves to be adjusted, so that both the transitional processes and the statistics of the disordered regime can be studied effectively. The flow rate is digitally monitored and computer controlled. To limit surface contamination and temperature fluctuations, the film plane is covered by a Plexiglas chamber which is about 10 cm high.

A system for perturbing the entrance flow rate at frequency f and amplitude A is based on applying small pressure variations to the entrance manifold. These perturbations can span a wide range in amplitude, waveform, and frequency. Forcing by external noise with various types of statistics can also be conveniently achieved. Small two-dimensional disturbances can also be generated at downstream positions by weak air flow from a tube which has a gap 0.5 mm wide along its length, placed transverse to the flow about 2–3 mm above the liquid film. However, the waveform of the perturbation is not controlled in this case.

Water and glycerin–water solutions (50% by weight) are used. The latter are less affected by surfactants adsorbed on the liquid film (Alekseenko *et al.* 1985). Also, two-dimensional waves on the surface of glycerin–water films are more stable against three-dimensional disturbances. We determined the viscosity of glycerin–water solutions (as a function of temperature) and surface tensions of both the solutions and the pure water, in order to compute the Reynolds and Weber numbers for each experiment. The viscosity of glycerin–water solutions at 22 °C is $\nu = (5.02 \pm 0.05) \times 10^{-6}$ m^2/s, the surface tension is $\gamma = (69 \pm 2) \times 10^{-3}$ N/m and its density is $\rho = 1.13$ g/cm^3. The surface tension of uncontaminated water is $\gamma = (72 \pm 2) \times 10^{-3}$ N/m. The working temperature varies by less than 0.4 °C in one run.

3.2. *Local measurement method and analysis*

Laser beam deflection is used as a local measurement method in our experiments to detect the waves and measure their properties, because of the high sensitivity that can be obtained in this way, and to avoid affecting the downstream waves by intrusive probes. Position-sensing photodiodes (PSPD's) are used to detect the deflection of

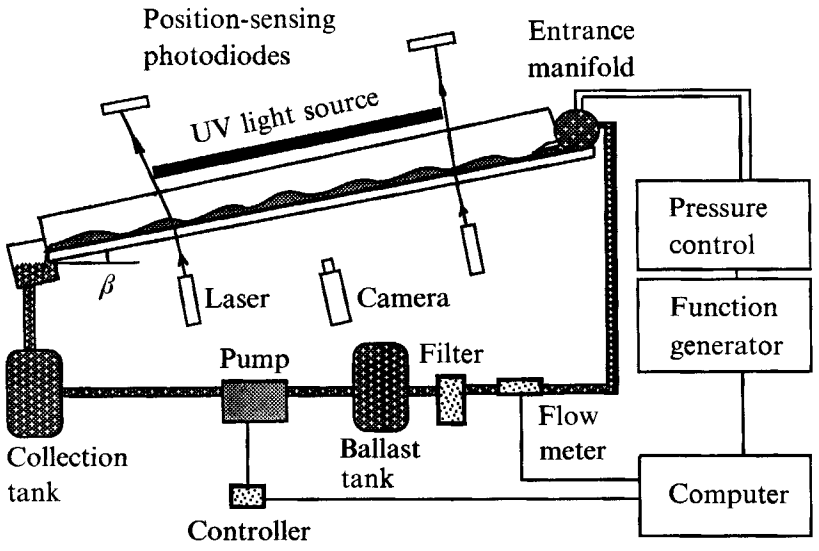

FIGURE 1. Schematic diagram of the film flow apparatus with variable inclination angle β, showing the automated flow control system with a ballast tank for noise reduction, the method of introducing periodic forcing of the input flow rate into the entrance manifold, and measurement methods based on laser beam deflection and fluorescence imaging.

normally incident laser beams (figure 1). This gives us a quantitative time series for the local wave slope $h_x(x_0, t)$. The resolution of this method is limited by electronic background noise, laser power fluctuations, and any small mechanical vibrations of the PSPD and the laser source. When the distance between the PSPD and the film plane is large (say 90 cm), the electronic noise becomes insignificant. We then find that the resolution of the wave slope measurements is approximately 5×10^{-5}. For sinusoidal waves with $\lambda = 5$ cm, this slope sensitivity corresponds to a wave amplitude of only 0.4 μm. In the absence of forcing, we find that fluctuations of the input film thickness (for example, due to mechanical vibrations) are smaller than this magnitude, i.e. 0.4 μm or less.

The following analysis is used to interpret the wave slope data. Assuming that two-dimensional waves consist of many spatial developing Fourier modes, we have

$$h(x,t)-1 = \sum_j \delta_j \exp[-\mathrm{Im}(\alpha_j)x]\exp[\mathrm{i}(\mathrm{Re}(\alpha_j)x-\omega_j t)], \tag{7}$$

where j stands for the jth Fourier mode, δ_j is the initial small amplitude. Here $\mathrm{Re}(\alpha_j)$ and $\mathrm{Im}(\alpha_j)$ are the real and imaginary parts, respectively, of the complex wavenumber; $-\mathrm{Im}(\alpha_j)$ is the spatial growth rate, and $\mathrm{Re}(\alpha_j)$ the real wavenumber. The angular frequency ω_j is real. Then the wave slope at $x = x_1$ as a function of time, $s(x_1, t)$, may be written as

$$s(x_1,t) = \frac{\partial h(x,t)}{\partial x}\bigg|_{x=x_1} = \sum_j \delta_j|\alpha_j|\exp[-\mathrm{Im}(\alpha_j)x_1]\exp[\mathrm{i}(\mathrm{Re}(\alpha_j)x_1-\omega_j t+\phi_j+\tfrac{1}{2}\pi)], \tag{8}$$

where $|\alpha_j|$ and ϕ_j are the modulus and the phase angle of α_j respectively.

The amplitude of the jth mode at x_1 is $A_j(x_1) = \delta_j \exp[-\mathrm{Im}(\alpha_j)x_1]$, and the amplitude of the wave slope of the jth mode is $S_j(x_1) = \delta_j|\alpha_j|\exp[-\mathrm{Im}(\alpha_j)x_1]$. Usually $|\mathrm{Re}(\alpha_j)| \gg |\mathrm{Im}(\alpha_j)|$ so we can let $|\alpha_j| = \mathrm{Re}(\alpha_j)$. This analysis shows that the power spectral components of the wave slope $s(x_1, t)$ are the products of the spectral

components of $h(x, t)$ and the moduli squared of the corresponding wavenumbers. If the wave is dominated by a single frequency, then two probes at different locations can be used to determine the spatial growth rate $-\mathrm{Im}(\alpha_j)$. If the waves are assumed to translate (over a limited distance) at speed c without change of shape, then the waveform and its second spatial derivative h_{xx} can be determined.

Two local probes are used to measure the *wave slope cross-correlation function*, which is defined as

$$C(x_1, x_2, t) = (\sigma_1 \sigma_2)^{-1} \int s(x_1, \tau)\, s(x_2, t+\tau)\, \mathrm{d}\tau, \tag{9}$$

where σ_1, σ_2 are the standard deviations of $s(x_1, t)$ and $s(x_2, t)$ respectively. We typically average power spectra over 2–3 minutes and cross-correlation functions over 4–6 minutes.

3.3. *Fluorescence imaging method*

Global space–time measurements are obviously required to distinguish correctly between the spatial and temporal dynamics for nonlinear waves. To accomplish this, we dope the fluid with a small concentration (about 100–200 p.p.m.) of dye that fluoresces under ultraviolet illumination, and digitize the resulting images. (We refer to this method as *fluorescence imaging*.) The illumination is provided by fluorescent 'black lights' oriented parallel to the flow direction and located above the lateral edges of the film plane. Our calibrations show that the liquid properties are essentially unaffected by the dye, and that the light intensity in the image plane is linear in the local thickness. A high-resolution CCD camera is used to obtain images with a minimum spacing in time of $\frac{1}{15}$ s. The camera is shuttered to minimize blurring due to the fluid motion.

For films about 1 mm thick, the image intensity is given by

$$I(x, y, t) = K I_0(x, y)\, h(x, y, t), \tag{10}$$

where $I_0(x, y)$ depends on the local illumination and possibly its angular distributions, and K is a constant. Calibrations show that (10) is accurate for our experiments. The function $I_0(x, y)$ is measured for a static film, and digital processing then gives $h(x, y, t)$ directly. This method is quantitative, though not as sensitive to very small-amplitude waves as shadowgraphic imaging. Still, the ratio $h(x, y, t)/h_0$ can be determined with measurement precision of about 1%, even without phase-sensitive averaging (see below). Several instantaneous fluorescence images and their wave profiles are given in figure 2 as examples of this method. Figure 2(*a*) shows nearly saturated periodic waves at a fairly high frequency, while (*b*) shows an example of nonlinear solitary waves with subsidiary wavefronts. Finally, (*c*) shows an example of natural (unforced) waves far from the source.

For two-dimensional periodic waves, phase-sensitive averaging can be used to further improve the measurement precision. This is very useful for very small waves with amplitude less than 10 μm. The system, when forced even weakly at a selected frequency, exhibits amplification almost solely at the forcing frequency. We can then match the forcing frequency with our acquisition frequency (15 Hz) so that the detected periodic waves have the same phase after some integer multiple of acquisition periods, and we can then average their images. For many forcing frequencies within the useful range, this integer multiple is small enough to make signal averaging feasible, with consequent reduction of the measurement noise by roughly a factor of three to about 3–4 μm. Further improvement would require a digitization system with more than 8 bits.

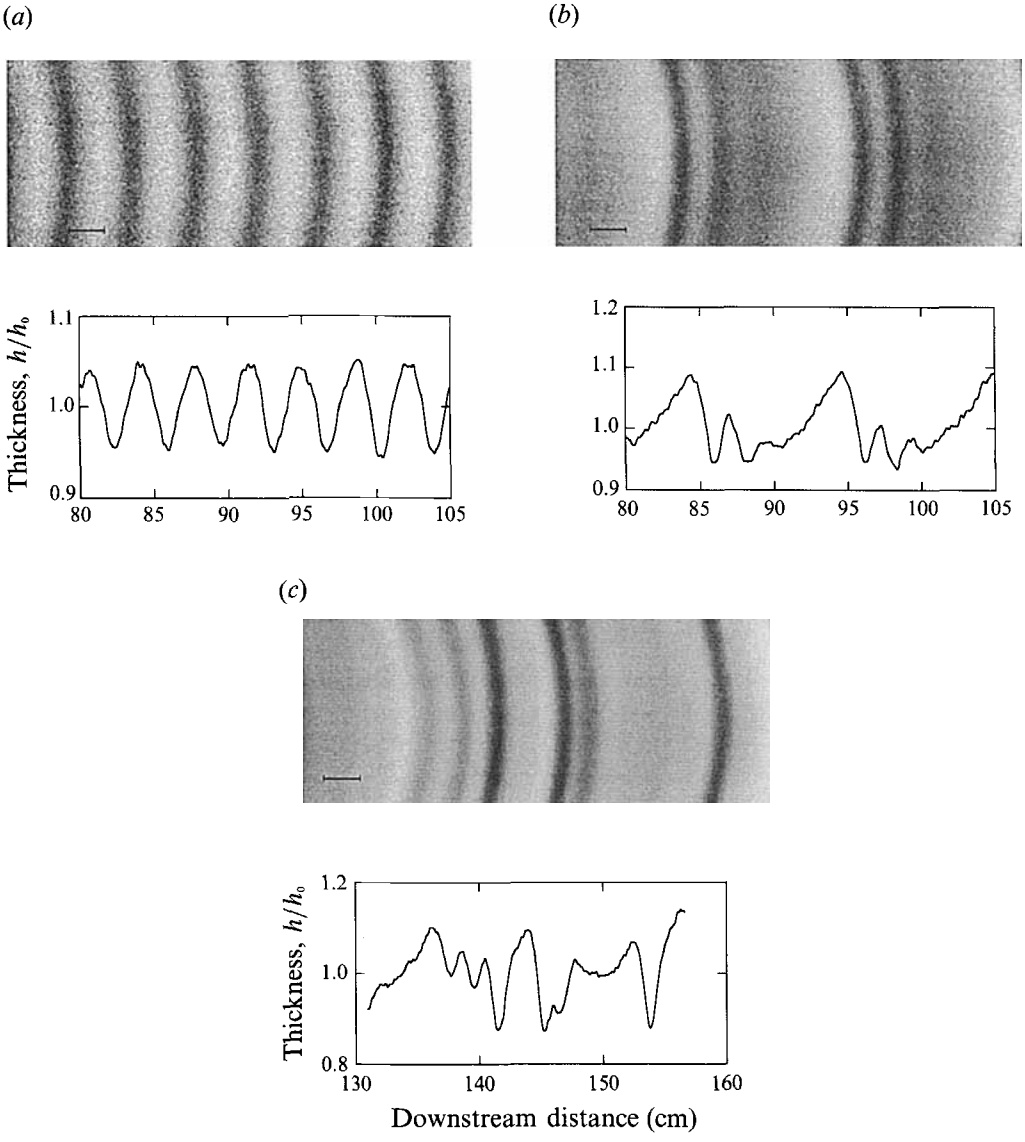

FIGURE 2. Fluorescence images of two-dimensional waves and their thickness profiles $h(x)$ (normalized by the mean thickness h_0), for water–glycerin films at $\beta = 4.6°$. The bar is 2 cm long. Films flow from left to right. The images have been digitally enhanced to increase the contrast. (*a*) Nearly saturated sinusoidal waves forced at $f = 5.5$ Hz, with Reynolds number $R = 25$. (*b*) Nonlinear evolution of low-frequency waves: subsidiary peaks have formed in front of the primary peaks ($R = 25, f = 2$ Hz). (*c*) Unforced natural waves far downstream ($R = 57$).

3.4. *Other technical issues*

Because we mainly study linear and weakly nonlinear properties of film flows near the critical point R_c, slow spatial variation of the wave structure is essential for us to investigate the spatial evolution and to distinguish different processes. Therefore we usually use small inclination angles (4°–8°) and moderate Reynolds numbers (< 60). For large angles very small R would be required; in this case film rupture disturbs the experiment because the films are too thin.

When the liquid exits from the inlet manifold, a certain distance is required for the free-surface velocity to approach its final value. The entrance length is approximately $L_e \sim h_0 R$ (Pierson & Whitaker 1977). We avoid the first 15–30 cm after the inlet, a distance that is considerably longer than this estimate.

Edge effects may exist, though the ratio of film thickness to channel width is only 0.002. We investigated the size of the edge effects by measuring the surface velocity of unperturbed film. Hollow ceramic spheres serve as tracers to measure the surface velocity $u_s(y)$ in a strip 30 cm wide near the centreline of the film plane. The particles are about 200 μm in diameter and their mean density is 0.7 g/cm^3. We find that the surface velocity has a maximum value at the centreline of the film plane and falls off slowly as the transverse or spanwise coordinate y is increased away from the centre. The maximum velocity is 5–10% larger than u_0 calculated from the total discharge. The velocity variation is less than 3% in a 10 cm wide centre region, and less than 9% over 20 cm.

Spanwise variation of the surface velocity may result not only from edge effects but also from slight non-uniformity of the film thickness. For example, film thickness variation of 3% (about 30 μm) can result in 6% variation in surface velocity. We noted that the curvatures of two-dimensional waves do not change significantly after the first 30–40 cm. The waves can then be treated as being essentially two-dimensional, over the central strip that is actually studied. We correct R near the centreline by use of the measured surface velocity.

4. Experimental results

We first describe the measurement of the critical Reynolds number for inclination angles up to 10°. Next we present experimental evidence that firmly establishes the convective nature of the instability and demonstrates that the resulting waves are noise-sustained structures. Finally, we discuss the nonlinear properties of periodic waves, their frequency dependence, and their instability. We mainly study two-dimensional waves in this paper (figures 8, 9 are exceptions).

4.1. *Measurements of the critical Reynolds number*

We have determined the critical Reynolds number R_c carefully as a function of inclination angle β. It is difficult to measure quantitatively, because the instability occurs at wavenumber $\alpha = 0$ at R_c. Therefore, it is necessary to measure the neutral stability curve $f_c(R)$ and to extrapolate it to zero frequency in order to determine R_c. Our method is as follows. Two position-sensing photodiodes separated by about 1 m in the streamwise direction and located 90 cm above the film are used to measure very small sinusoidal waves that are forced at frequency f. The amplitudes of the wave slope variations at two positions are determined from the power spectra by measuring the area under the peak at the forcing frequency. Fixing β and R, we compare the two amplitudes at different f to find the cutoff frequency f_c for which the waves neither grow nor decay. This frequency is determined by fitting curves to the data from the two probes, and locating their intersection as shown in figure 3. The cutoff frequency can typically be determined to a precision of about 0.2 Hz.

This measurement of the cutoff frequency is made at many Reynolds numbers near the onset of instability. The data for $f_c(R)$ are then fitted to a square root function of $(R-R_c)$ near the critical point, as suggested by linear stability analysis (see (6)):

$$f_c = a(R-R_c)^{\frac{1}{2}}, \tag{11}$$

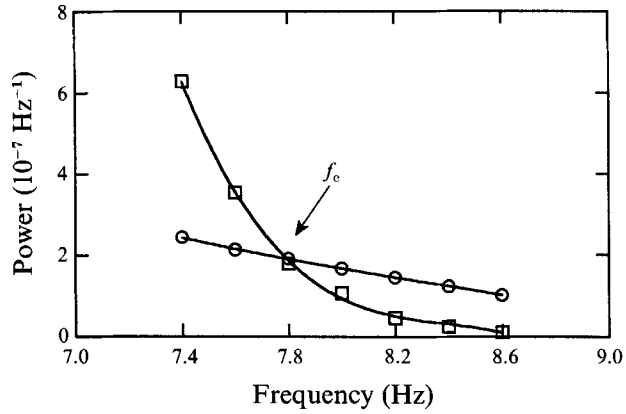

FIGURE 3. Determination of the cutoff frequency f_c from the integrated spectral power of the wave slope near the forcing frequency at two spatial locations, $x = 43$ cm (○), $x = 134$ cm (□), as functions of the forcing frequency. The data are for glycerin–water films with $\beta = 5.6°$ and $R = 20.7$. The intersection point leads to the measurement of f_c as 7.8 Hz under these conditions.

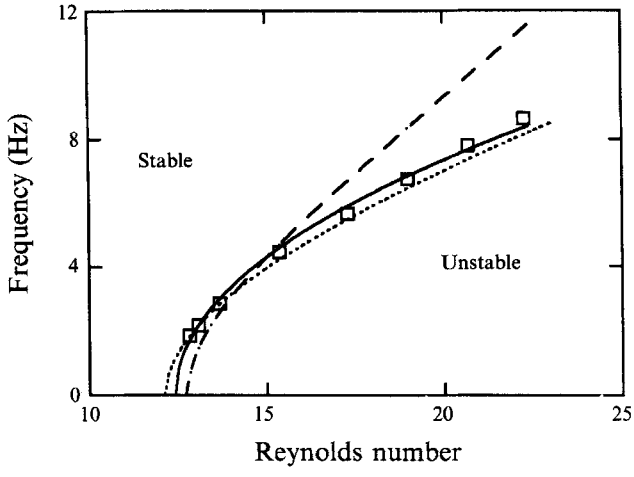

FIGURE 4. Neutral stability curve for glycerin–water films at $\beta = 5.6°$: the cutoff frequency f_c is shown as a function of Reynolds number, along with a fit (solid line) to (11). R_c is determined to be 12.4 ± 0.1. The theoretical value is 12.7 for $\beta = 5.6°$. The dashed line is the linear solution of (5), and the dotted line is the solution to (3).

where R_c and a are fitting parameters. Equation (11) should be asymptotically valid near R_c. The fitted function gives the critical value R_c as shown in figure 4 (solid curve). The dashed line is the linear solution of the Benney equation (5) based on experimental parameters. It is clear that (5) is not valid for large R. The dotted line is the solution to the Orr–Sommerfeld equation (3) by the method of Anshus & Goren. We note that f_c depends on surface tension but the final result for R_c is independent of the liquid properties.

The entire procedure is then repeated for many angles β. Results for the critical Reynolds number for both pure water and glycerin–water solutions are shown in figure 5. The data are compared with the theoretical prediction $R_c = \frac{5}{4}\cot\beta$, given by the solid line. We find good agreement, with a standard deviation (relative to the theoretical

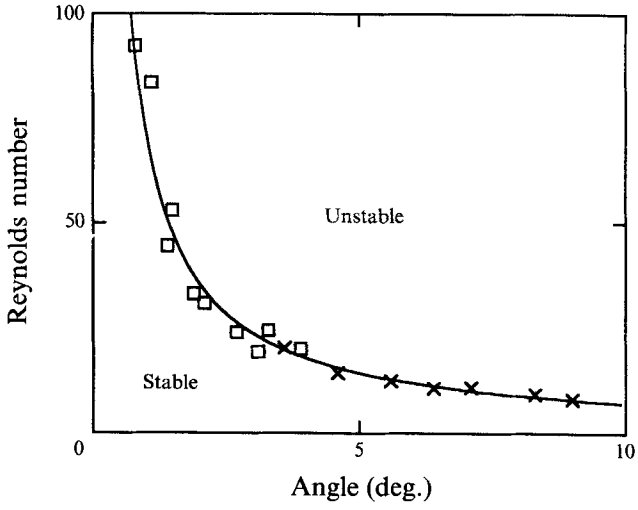

FIGURE 5. Critical Reynolds number R_c as a function of inclination angle β. Results from both water (□) and glycerin–water solutions (×) are shown. The solid line is (4).

curve) of about 10%. Because of the complex procedure that is required to obtain the data, the measurement precision is probably no better than this. We conclude that the agreement is quite satisfactory, and this implies that physical approximations made in the formulation of the stability theory are correct at least near the critical point. These include the neglect of air flow above the fluid, the formulation of the boundary conditions, and the use of the semi-parabolic velocity profile. We can also conclude that the long-wave expansion equation (5) is adequate for R very close to the onset of instability.

4.2. *The convective character of the instability*

Linear analysis predicts that the primary instability of film flows should be convective at least near the critical Reynolds number. It is unclear theoretically whether it remains convective at higher R. To study the nature of the instability experimentally we investigate the response of film flows to external perturbations. Our results demonstrate that film flows are convectively unstable over the entire range we could conveniently explore, up to about $R = 200$ for $\beta < 10°$.

In figure 6 we show simultaneous wave slope data at two positions to illustrate the propagation of small pulses. Figure 6(*a*, *b*) shows that a pulse generated at the entrance reaches a probe at $x = 44$ cm with quite small amplitude, and about 1.5 s later it reaches a more distant probe (at $x = 97$ cm) with an amplitude larger by more than a factor of 10. However, the pulse is amplified only in a frame of reference moving with the wave. The film at a fixed location resumes its previous state after the pulse passes. This is the typical character of a convective instability. It also demonstrates that the waves have to be sustained by external perturbations. To emphasize the fact that perturbations do not travel upstream, we show the results of perturbing the film near the centre of the apparatus (at $x = 69$ cm). Both forward and backward pulses are generated; the forward pulse shows characteristics similar to figure 6(*a*, *b*), but the backward pulse is progressively damped (figure 6*c*, *d*). Wave packets can only persist on the film surface in the forward direction.

We first studied the sensitivity of film flows to external periodic forcing introduced at the entrance in order to understand the role of natural noise, which always exists at

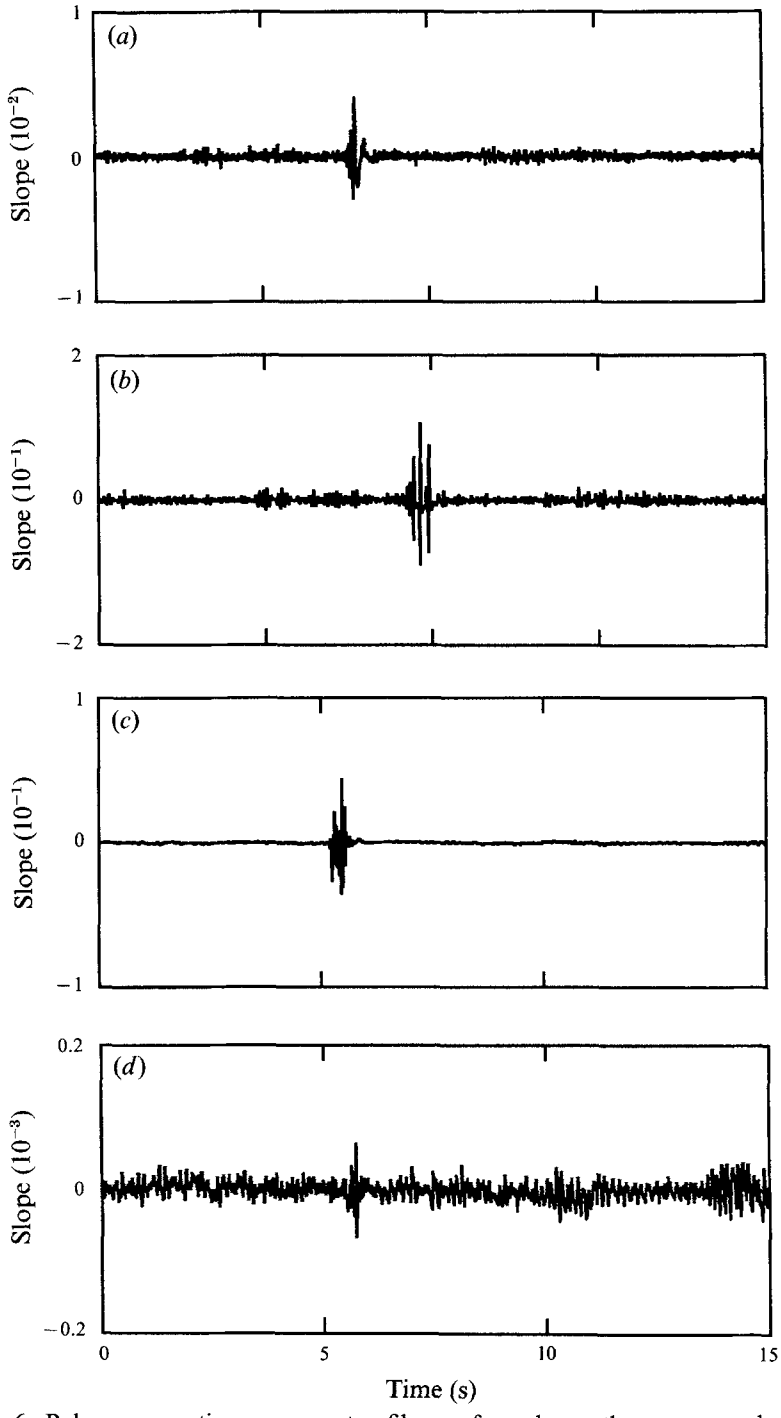

FIGURE 6. Pulse propagation on a water film surface shows that wave packets are amplified downstream only ($\beta = 2.5°$). A pulse generated at the entrance is observed (*a*) at $x = 44$ cm and (*b*) at $x = 97$ cm ($R = 150$). The backward strongly attenuated propagation of a pulse generated at $x = 69$ cm is shown in (*c*) at $x = 61$ cm and (*d*) at $x = 50$ cm ($R = 91$). Note that the vertical scales are different.

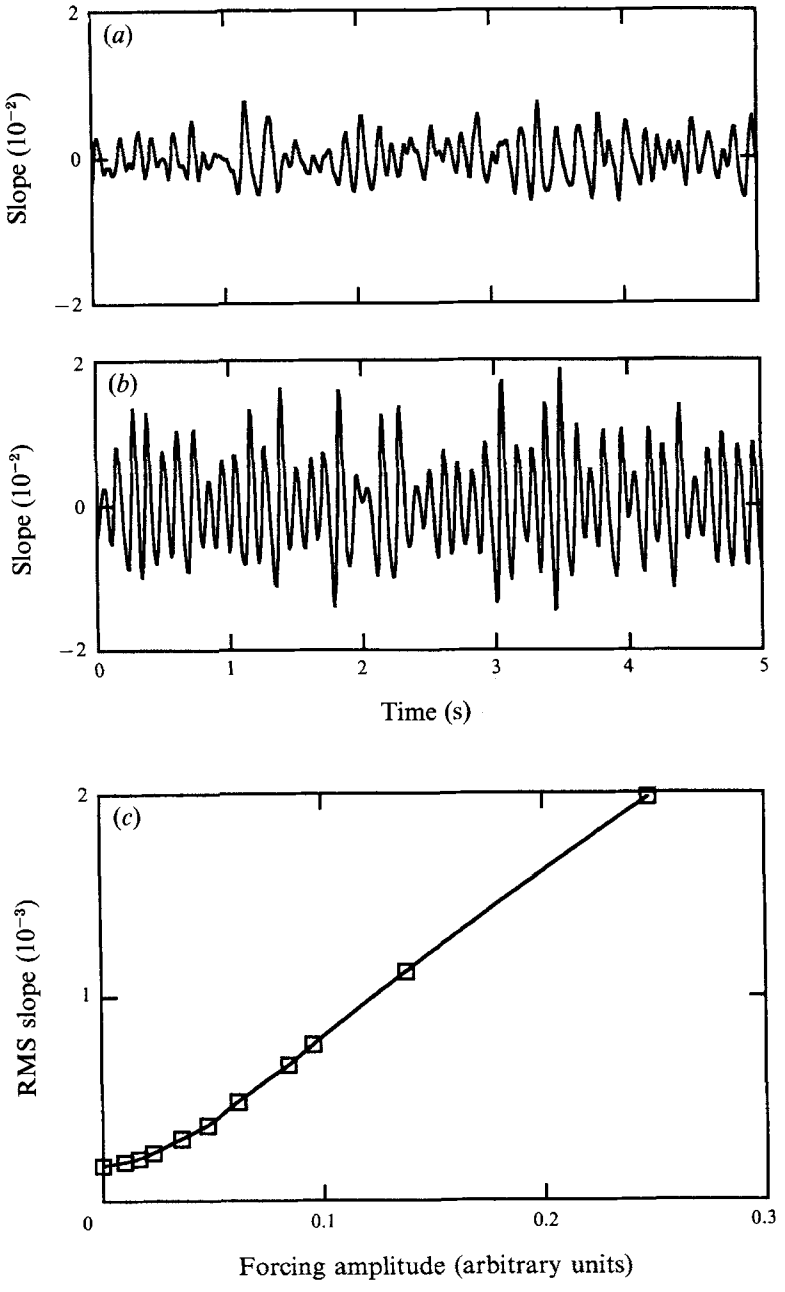

FIGURE 7. Response to periodic forcing of water films, showing strong sensitivity to external signals ($\beta = 2.5°$, $R = 150$). Slope *vs.* time at $x = 97$ cm, (*a*) without and (*b*) with forcing ($f = 9$ Hz). (*c*) Root-mean-square wave slope at $x = 44$ cm as a function of the forcing amplitude ($f = 9$ Hz).

some level. Natural noise is amplified downstream, as shown in figure 7(*a*). When a small sinusoidal perturbation is applied, the wave amplitude is larger and the waves are more regular (figure 7*b*), though the effects of the natural noise are still evident in the waveform. The smooth transition from noise-driven to periodically forced waves is illustrated by the response curve of figure 7(*c*) which shows the root-mean-square

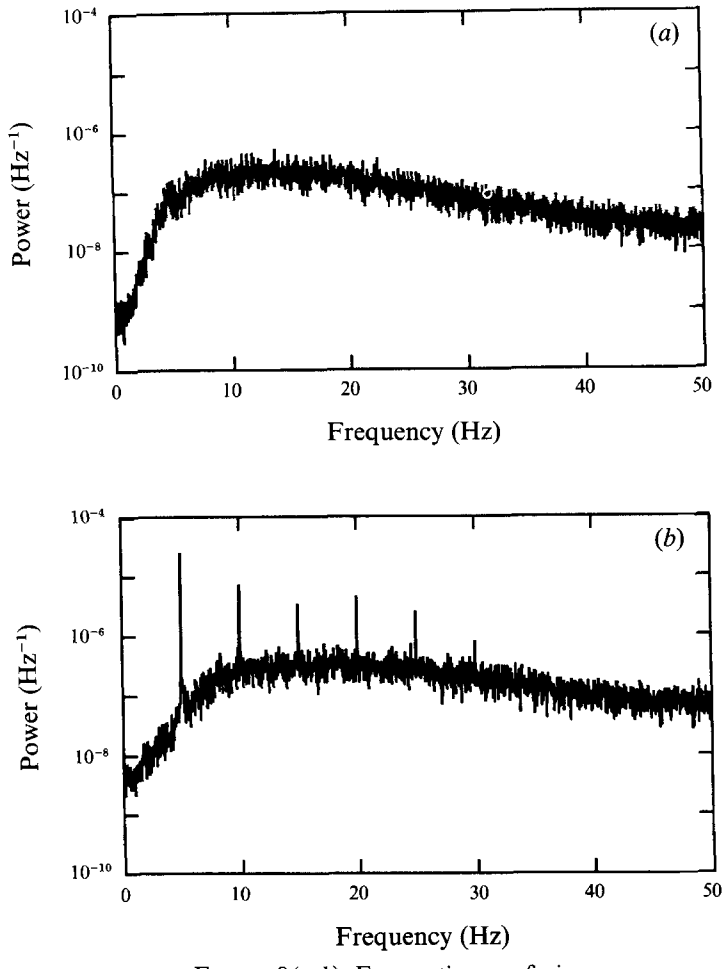

FIGURE 8(*a*,*b*). For caption see facing page.

(RMS) value of the wave slope versus the strength of the periodic forcing. Once the forcing is larger than the natural noise, the response is linear. We conclude that film flows are sensitive to external forcing or to noise.

Sufficiently far downstream, the waves are larger and more nonlinear. In this regime, the waves are statistically independent of the nature of the forcing. An example is shown in figure 8, which shows power spectra of the local wave slope at $R = 115$ and $\beta = 4.1°$ for water, with and without periodic forcing, at an upstream location (figure 8*a*, *b*) and at a downstream location (figure 8*c*, *d*). In the upstream case, the periodic signal and the natural spectrum are essentially additive. In the downstream case, the spectra are essentially independent of the presence or absence of the periodic forcing. Here, the waves are quite three-dimensional and have complicated wave fronts, as shown in figure 9. This implies that external noise initiates and sustains the waves but that the nature of the forcing becomes unimportant once the nonlinear dynamics has acted on the waves for a sufficient distance (in the laboratory frame) or time (in the moving frame).

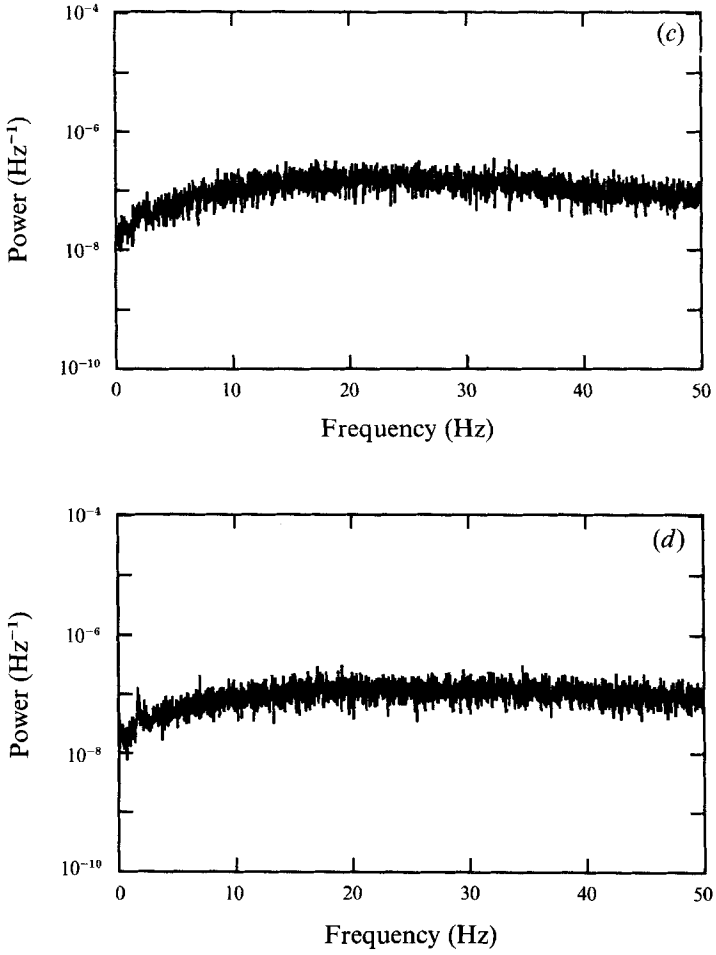

FIGURE 8. Power spectra of the wave slope for natural waves on water films (a, c), and for waves forced at 5 Hz (b, d) at different distances downstream ($\beta = 4.1°$, $R = 115$). Far from the source, the nonlinearity is strong, and the waves become independent of the forcing. (a, b) $x = 79$ cm; (c, d) $x = 155$ cm.

4.3. *Properties of the noise-sustained (natural) wave patterns*

We studied the evolution of the wave slope time series and its spectrum as a function of distance down the film plane, and the results are given in figures 10 and 11. (A glycerin–water solution is used, with $\beta = 6.4°$ and $R = 27$.) The waves are unforced, and result from the amplification of ambient noise, which produces RMS fluctuations of only 5×10^{-5} in the wave slope at a distance of 16 cm from the source (figure 10*a*). These spontaneous waves are spatially developing two-dimensional non-periodic waves. They grow by almost three orders of magnitude over a distance of 144 cm, and their frequency content changes, as shown by the spectra of figure 11. Near the inlet, the wave spectrum is broadband and roughly exponential (figure 11*a*). The waves are selectively amplified as they travel downstream, thus causing the time series to be more regular (figure 10*b*) and the spectrum to be narrowed (figure 11*b*). It is interesting to note that the mean frequency (4.0 Hz) of the waves at this position ($x = 80$ cm) corresponds closely to the most strongly amplified frequency predicted by linear stability theory ($f_m = 3.9$ Hz).

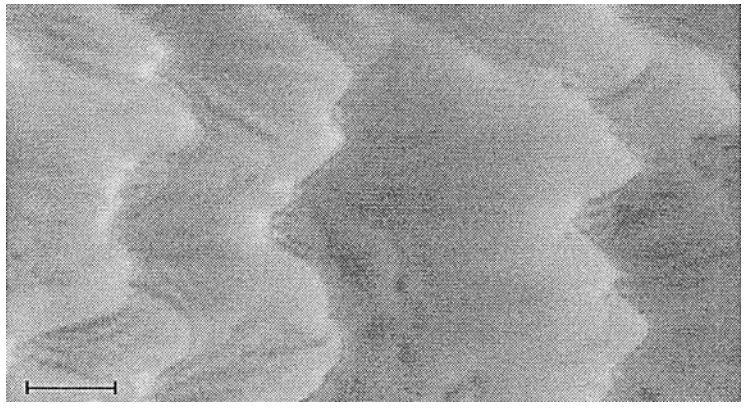

FIGURE 9. Fully developed natural waves on a water film, far from the source ($\beta = 10°$, $R = 113$). The film flows from left to right. The left side of the fluorescence image is near $x = 142$ cm. The bar is 4 cm long.

Nonlinearities become important for $x > 90$ cm, and sharp dips are noted in the wave slope (figure 10*c*); these correspond to the development of steep wave fronts. The spectrum also broadens significantly (figure 11*c*). The development of steep wavefronts is accentuated in the last panel, figure 10(*d*), which is taken 160 cm from the source. The power spectrum here decays exponentially at high frequencies. The waves remain essentially two-dimensional through this entire series of events, though presumably the glycerin–water solutions eventually become three-dimensional for sufficiently large R and x, as the pure water films do.

In order to establish the extent to which the waves at a particular location are correlated with the waves upstream at that point, we computed cross-correlation functions between the slope time series at different spatial points x_1 and x_2 as a function of the lag time, as defined in (9). In the linear and transitional regions, the time series of the wave slope at the downstream point x_2 is strongly correlated with that at the upstream point x_1, with the maximum correlation occurring at a delay equal to the propagation time (figure 12). This fact implies that the downstream waves are the direct result of ambient noise at the entrance and upstream positions. However, as the degree of nonlinearity increases, the correlation fades (not shown) until there is very poor correlation between upstream and downstream locations for fully developed cases at high R.

The results of §§4.2 and 4.3 may be summarized as follows. We find that film flows are sensitive to external perturbations: the waves are initiated and sustained by external noise. As a function of distance x from the source at fixed R we may distinguish several distinct regimes. First, the *linear region* is characterized by the frequency-selective amplification of external noise. In the *transitional region* nonlinearity renders the effect of the input noise progressively less important, until finally a *fully developed wave state* is reached in which the nonlinear dynamics completely dominates the initial disturbances. This behaviour is very similar to the generic behaviour of model systems showing convective instabilities, such as the Ginzburg–Landau equation (Deissler 1987*a*). The phenomena are quite different from those observed in systems having an absolute instability, where external noise plays a much smaller role except near the threshold.

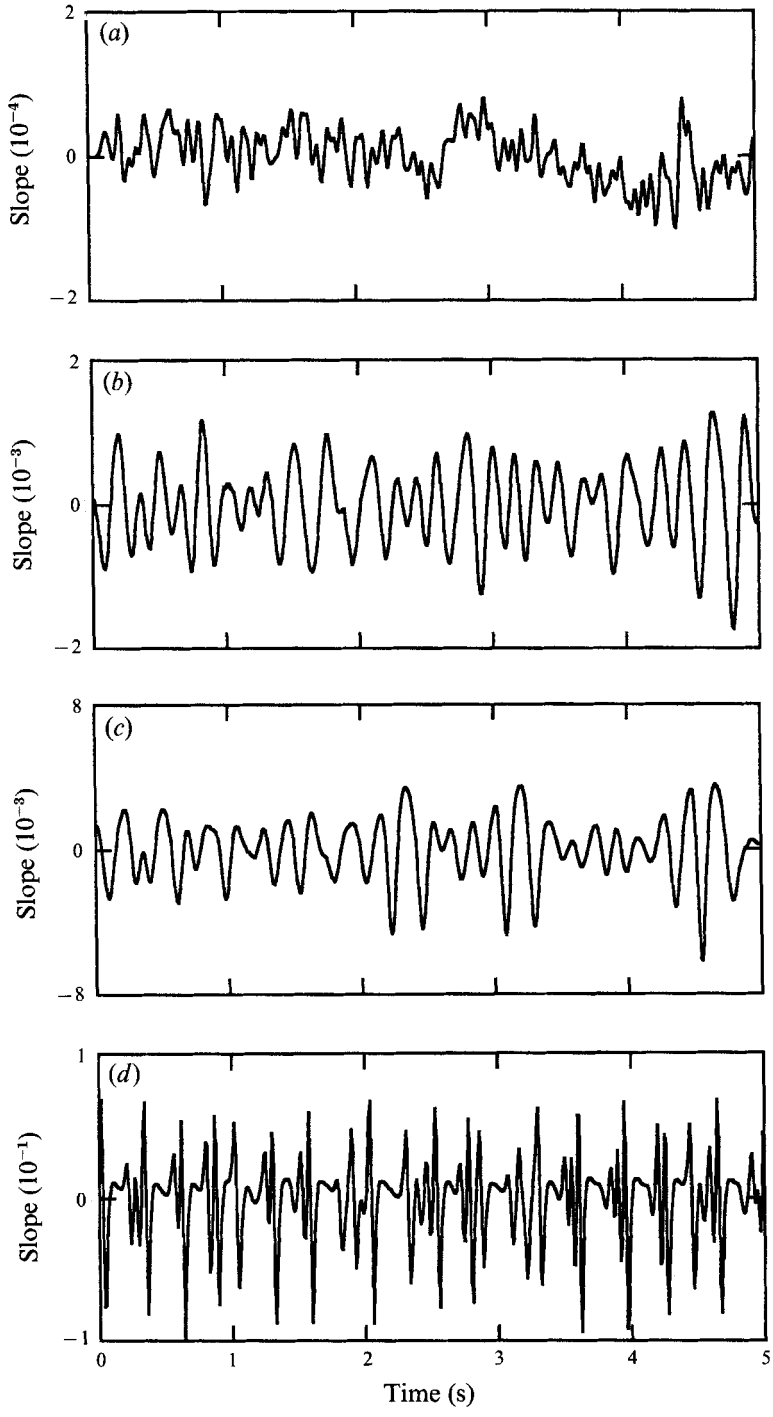

FIGURE 10. Noise-sustained structure: time series of the wave slope for natural waves on glycerin–water films ($\beta = 6.4°$. $R = 26$). (*a*) $x = 16$ cm; (*b*) $x = 80$ cm; (*c*) $x = 96$ cm; (*d*) $x = 160$ cm.

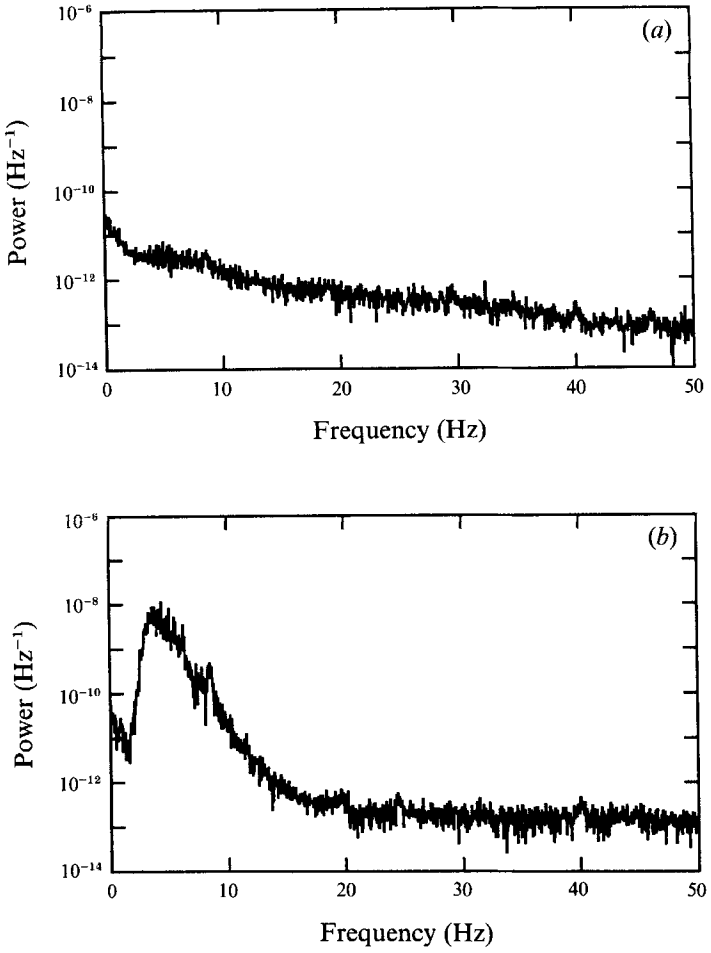

FIGURE 11(*a*,*b*). For caption see facing page.

4.4. *Precision measurements of spatial growth of periodic waves*

It is helpful to study the evolution of sinusoidal perturbations in order to fully understand the internal dynamics of film flows. We use the fluorescence imaging method to measure the spatial growth rate and phase velocity for small-amplitude sinusoidal waves, at modest inclination angles and Reynolds numbers. These measurements extend previous work by Krantz & Goren (1971*a*), who used local probes to study wave growth over a more limited range of parameters. The spatial growth measurements also test the quantitative validity of our fluorescence imaging method. We choose forcing frequencies such that signal averaging (§3.3) can be used to improve the measurement precision. The measured wave profiles are then fitted to the following functional form for spatially growing sinusoidal waves:

$$h(x,t)-1 = \delta \exp[-\mathrm{Im}(\alpha)\,x]\sin[\mathrm{i}(\mathrm{Re}(\alpha)\,x-\theta)], \tag{12}$$

where δ is the initial amplitude, α is the complex wavenumber and θ is the phase. From the fitting constants we determine the spatial growth rate $[-\mathrm{Im}(\alpha)]$, the wavenumber $[\mathrm{Re}(\alpha)]$, and the phase velocity. This functional form provides an excellent fit for small-amplitude waves. An example is shown in figure 13, for a glycerin–water solution, at

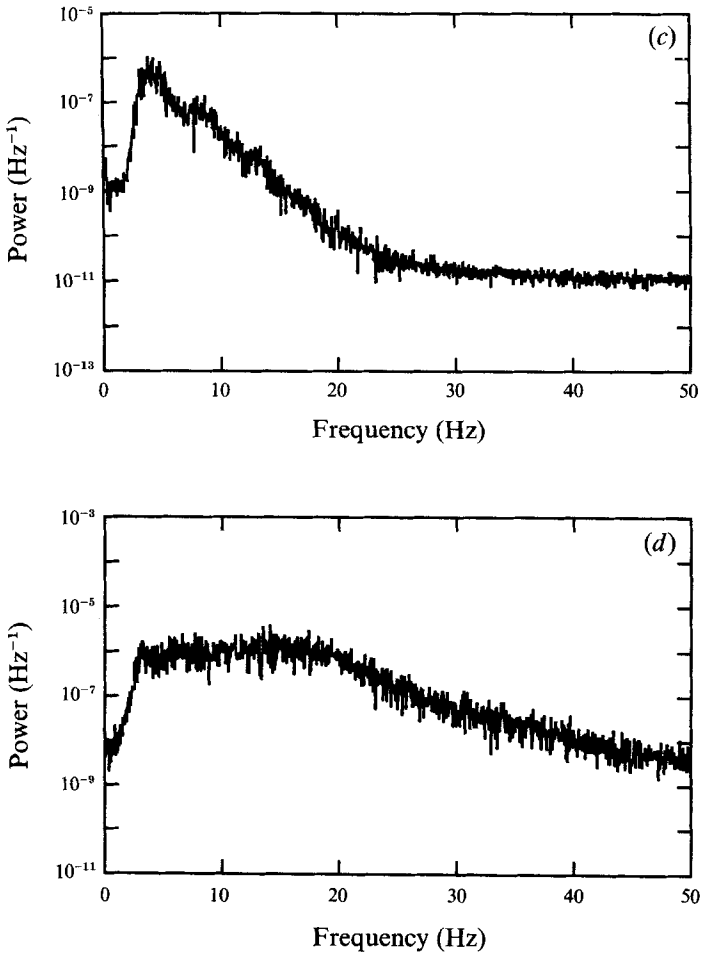

FIGURE 11. Noise-sustained structure: power spectra of the wave slope time series (from figure 10) ($\beta = 6.4°$, $R = 26$). (*a*) $x = 16$ cm; (*b*) $x = 80$ cm; (*c*) $x = 96$ cm; (*d*) $x = 160$ cm. After an initial stage of narrow-band amplification, nonlinearities become important and broaden the spectrum.

$\beta = 4.6°$, $R = 23$, and $f = 5$ Hz. Here, the 'initial amplitude' δ is 0.2% of the average film thickness $h_0 = 1.12$ mm, i.e. about 2 μm, while the wave amplitude at $x = 90$ cm is about 14 μm, less than 2% of h_0. The standard deviation with respect to the best fit is about 2% of the wave amplitude. However, when the amplitude becomes large, the wave profiles deviate significantly from (12) because of nonlinearity. We restrict our analysis in this section to the linear regime.

In figure 14, we present the measured dimensionless growth rate and phase velocity for glycerin–water films with $\beta = 4.6°$, $R = 23$ and $W = 62$. We compare the measurements to a solution of the Orr–Sommerfeld equation (3) calculated by the method due to Anshus & Goren (1966). The growth rate is in good agreement with theory, with no adjustable parameters. In particular, the wavenumber for fastest growth is correctly predicted. The velocity has the same shape as the theoretical curve, but is about 3–5% larger. The small deviation may be a finite-amplitude effect. The dashed line in figure 14 is the linear result of the Benney equation (5). This comparison demonstrates that (for $R \approx 23$) equation (5) is only valid for very long wavelengths. In general, these results confirm the approximations made in the linear theory and also

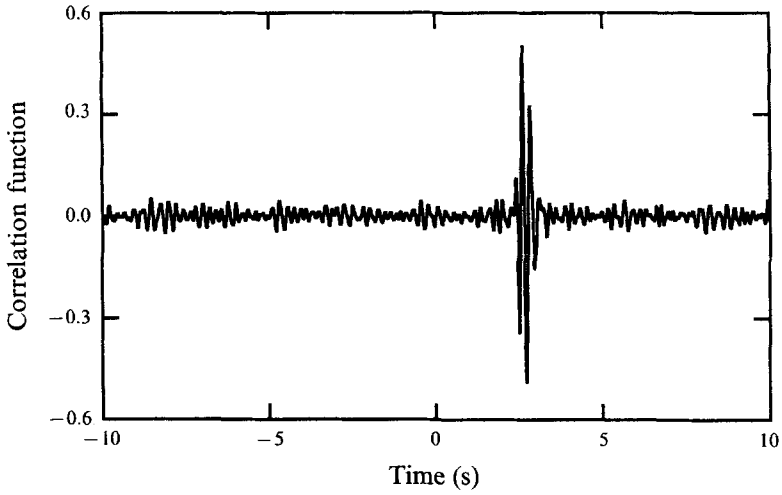

FIGURE 12. Spatial cross-correlation function $C(x_1, x_2, t)$ of the wave slope for natural waves under the same conditions as figure 10, for $x_1 = 37$ cm, $x_2 = 96$ cm. The waves are strongly correlated in the linear region, but the correlation decreases (not shown) for waves far from the source.

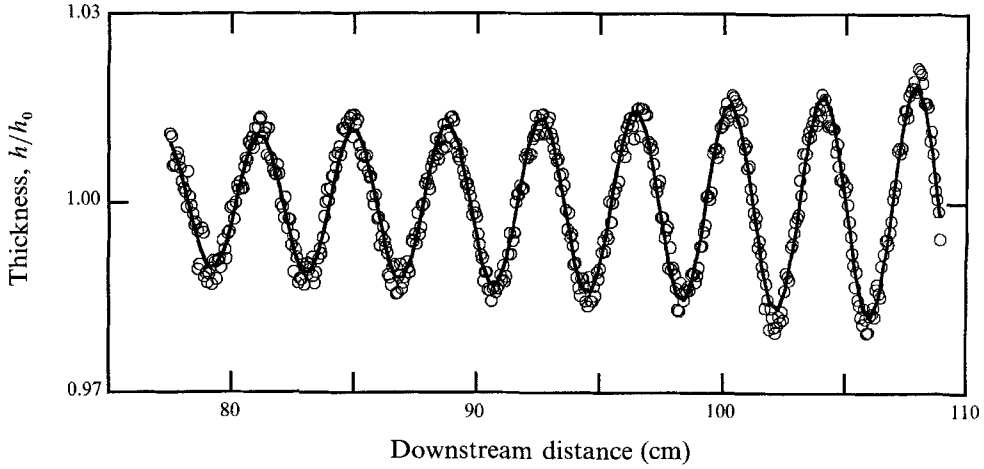

FIGURE 13. Exponential growth of a sinusoidal wave on a glycerin–water film ($\beta = 4.6°$, $R = 23$, $f = 5$ Hz). The circles are data taken from digitized images after signal averaging, and the solid line is the fitting curve (equation (12)). The fitting constants are: dimensionless spatial growth rate $[-\mathrm{Im}(\alpha)] = 2.3 \times 10^{-3}$, wavelength $\lambda = 3.82$ cm, and dimensionless phase velocity $c = 1.9$.

show that the fluorescence imaging method can be used to study film flows quantitatively. The process used to obtain the data in figure 14 is extremely time consuming, so we have not varied β and R systematically, though similar results were obtained for several other cases.

4.5. *Nonlinear evolution*

In this subsection and the following one, we describe studies of the nonlinear evolution of wavy films using both the fluorescence imaging method and local probes. Weakly nonlinear theory (see §2.4) indicates that there should be a phase boundary $\alpha_s(R)$ $(0 < \alpha_s(R) < \alpha_c(R))$ which separates two regions dominated by distinct bifurcations. This transition appears not to have been previously measured.

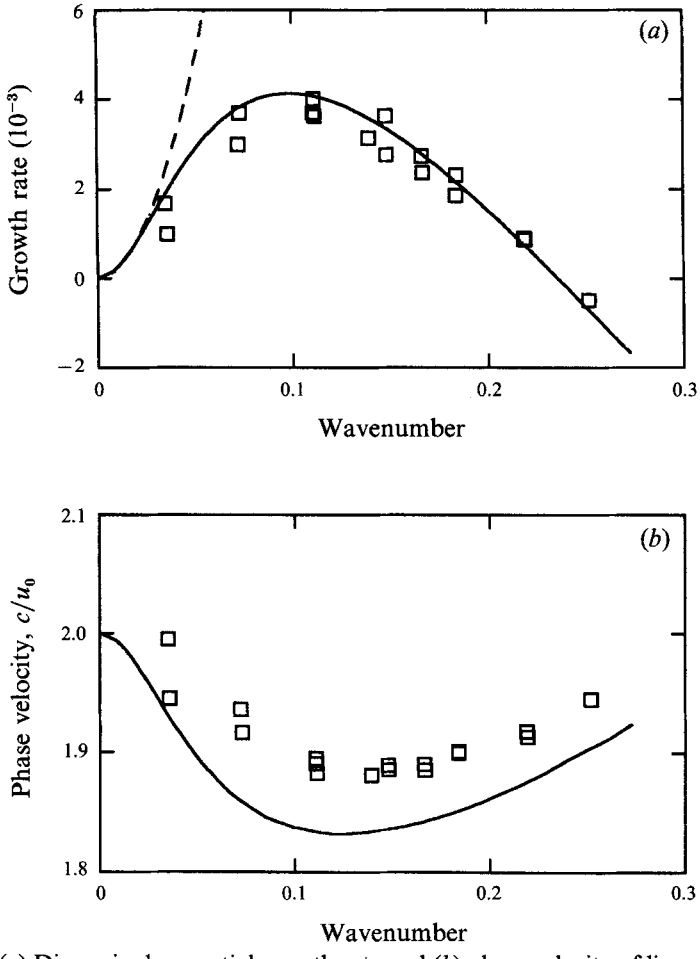

FIGURE 14. (*a*) Dimensionless spatial growth rate and (*b*) phase velocity of linear waves as functions of wavenumber, for glycerin–water films with $\beta = 4.6°$, $R = 23$ and $W = 62$ (here $\gamma = 69 \times 10^{-3}$ N/m, $\nu = 4.89 \times 10^{-6}$ m^2/s). The solid lines are linear predictions computed with the method due to Anshus & Goren (1966). The dashed line in (*a*) is the linear result of (5).

The experiments described in this section indicate that the transition may be identified with the wavenumber below which multipeaked solitary waves are produced instead of saturated nearly sinusoidal waves. We illustrate the transition by means of the wave profiles shown in figure 15. The measurements were made using the fluorescence imaging method with signal averaging. The thickness has been scaled by h_0. The four panels show the wave evolution for successively larger values of the frequency (or wavenumber).

In the first case (figure 15*a*) the forcing frequency is only 1 Hz, and the wave profiles are shown at equally spaced times $\frac{2}{15}$ s apart, with each profile displaced vertically from the previous one for clarity. As the amplitude increases, the wave shape departs considerably from sinusoidal form. The crests are well separated and develop steep fronts and stretched tails. Subsidiary wavefronts nucleate successively while the primary peaks grow more slowly. Power spectra of the local wave slope (not shown) reveal the fast growth of higher harmonics during the generation of solitary waves. If the waves are not unstable to three-dimensional disturbances (as for these glycerin–water films), quasi-stationary 'multipeaked solitary waves' are observed. For

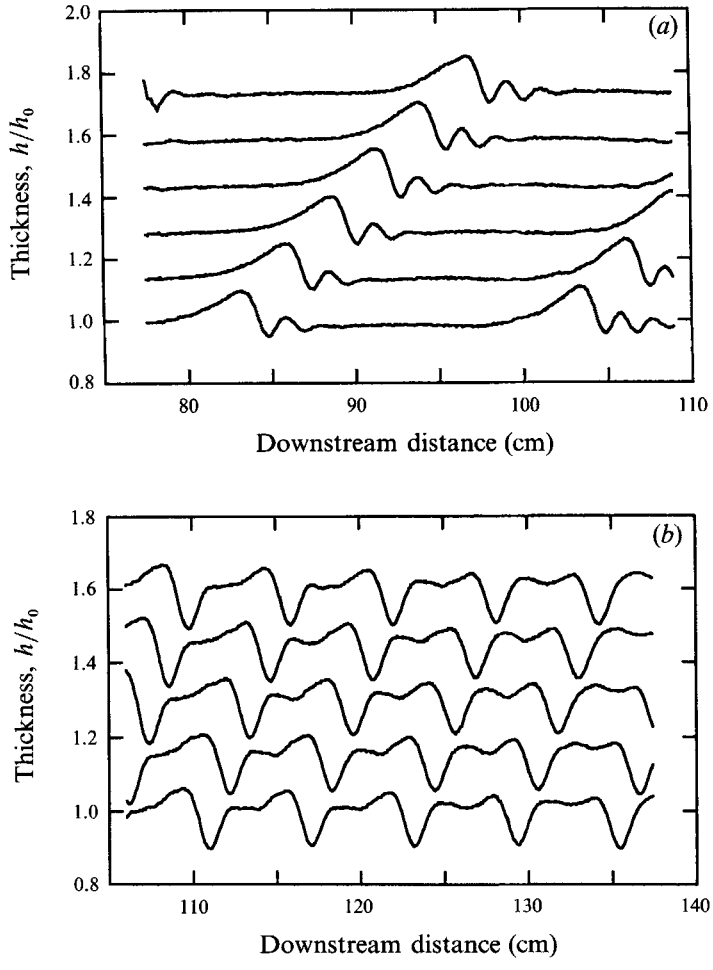

FIGURE 15(*a*,*b*). For caption see facing page.

very low frequency, the distance between two solitary waves is so large that new waves develop between them. Three-dimensional instabilities eventually occur, a process that apparently involves interaction between the primary and subsidiary peaks.

If the forcing frequency is increased to 3 Hz (figure 15*b*), the primary wavefronts are closer together, and clearly separated solitary waves are not formed. However, the waves still generate additional maxima, as indicated by the double-peaked structure ('breaking') in figure 15(*b*). We note that $f = 3$ Hz is larger than the fastest growing frequency ($f_m \approx 2.6$ Hz) predicted by linear theory for the conditions in figure 15. When the frequency is increased to 4 Hz (figure 15*c*), there are no subsidiary maxima and the waves saturate in amplitude provided that three-dimensional instabilities and disturbances from amplified noise do not occur. However, the saturated waves are clearly non-sinusoidal, with steep dips separating rather flat maxima. As the frequency is increased towards the cutoff frequency, the waves become more nearly sinusoidal (figure 15*d*).

The saturation of high-frequency waves may also be demonstrated quantitatively by local measurements. Figure 16(*a*) shows the RMS wave slope as a function of the forcing amplitude for a fixed forcing frequency. When the forcing amplitude is small, the wave amplitude increases linearly with the perturbation amplitude. The

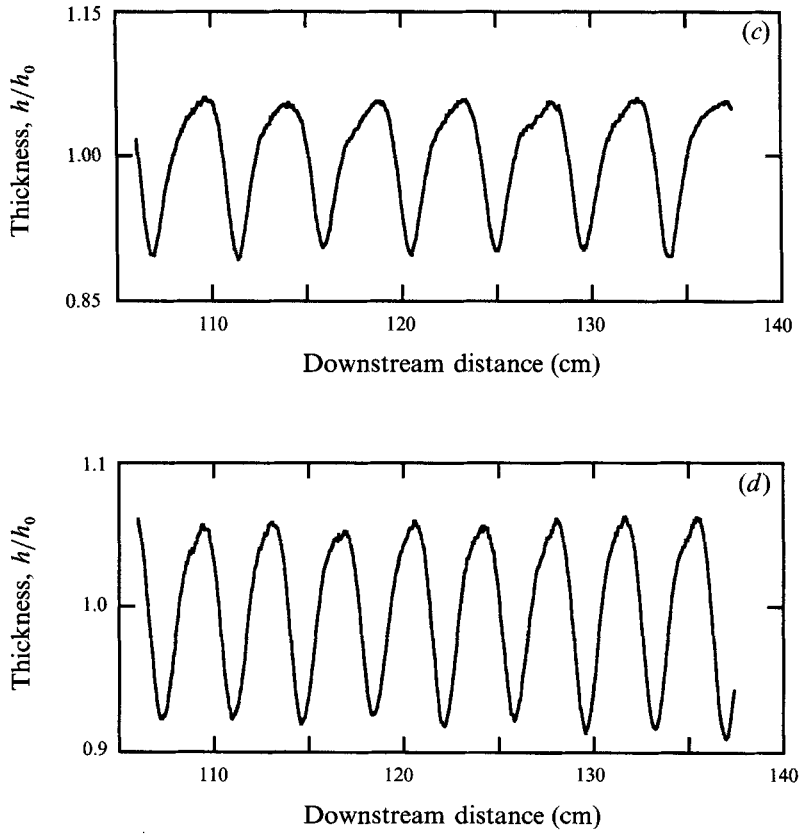

FIGURE 15. Wave profiles with signal averaging for glycerin–water films at $\beta = 4.6°$ and $R = 23$, showing the effect of varying the forcing frequency: (*a*) $f = 1$ Hz; profiles of multipeaked solitary waves are shown at $\frac{2}{15}$ s intervals, offset vertically for clarity. The nucleation of a new subsidiary peak is visible. (*b*) $f = 3$ Hz; profiles are shown at $\frac{1}{5}$ s intervals. (*c*) $f = 4$ Hz; saturated waves with steep dips and flat maxima. (*d*) *at* $f = 5$ Hz, the waves are more nearly sinusoidal.

downstream waves saturate if the forcing amplitude is made sufficiently large. The same phenomenon may be viewed differently by measuring the RMS wave slope for a fixed forcing amplitude, as a function of downstream distance. This quantity is shown in figure 16(*b*). The waves grow exponentially at first and then saturate downstream.

4.6. *A new phase boundary*

The laser beam deflection method is very sensitive, so we use local probes to measure the phase boundary $f_s^*(R)$ between saturated waves and multipeaked waves. (We use the asterisk on f_s here to distinguish the measured boundary from the theoretical one predicted by weakly nonlinear theory.) Large-amplitude forcing is used and the probes are set far downstream to minimize errors due to the finite length of the film plane. When we vary the frequency near the transition point $f_s^*(R)$ at constant forcing amplitude, we find that the transition is continuous. This makes it difficult to detect the boundary, so we use the following criterion. The second derivative of h with respect to x changes its sign at least four times in one period for 'breaking' waves and twice for saturated waves. Because the surface curvature is proportional to the second spatial derivative of the thickness h_{xx}, the sign of h_{xx} has the physical significance of indicating whether the surface tension force points out of or into the film.

To find the boundary $f_s^*(R)$ we differentiate h_x with respect to x to obtain h_{xx} by

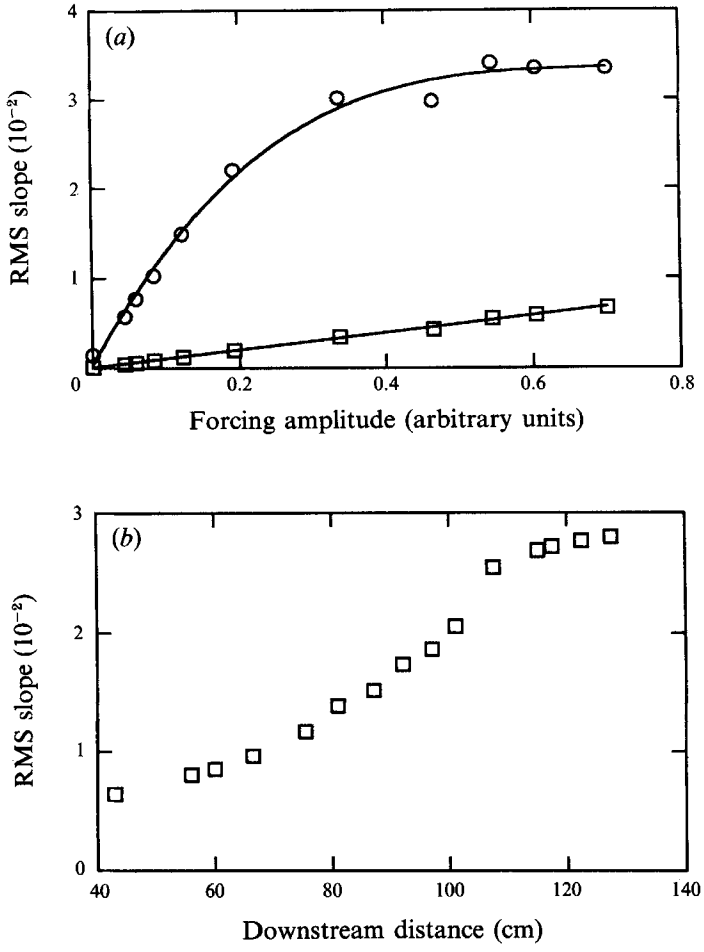

FIGURE 16. Wave saturation for sufficiently high forcing frequency: (*a*) RMS wave slope as a function of forcing amplitude (pure water, $\beta = 3.9°$, $R = 43$ and $f = 9$ Hz, $x = 31$ cm (□), $x = 91$ cm (○)); (*b*) RMS wave slope as a function of downstream distance (glycerin–water solutions, $\beta = 5.6°$, $R = 23$ and $f = 6$ Hz).

assuming that the waves translate without much change of shape. Since we are only concerned about the sign of h_{xx}, this is a satisfactory assumption. When we increase the forcing frequency from $f < f_s^*(R)$ to $f > f_s^*(R)$ at constant forcing amplitude, the phase orbit changes from that shown in figure 17(*a*) to that of figure 17(*d*) in the (h_x, h_{xx})-plane. The small loop in figure 17(*a*) is due to a subsidiary maximum. (It can also indicate a 'dimple' on the trailing edge when f is slightly below $f_s^*(R)$.) The loop becomes a cusp as f is increased. Figure 17(*b*, *c*) shows a magnified view near the cusp to clearly illustrate the transition, which is taken to be the frequency at which the extra zero crossings of h_{xx} are lost. We determine $f_s^*(R)$ based on several independent runs for each Reynolds number using different forcing amplitudes. In this way, we are able to locate the stability boundary within a precision of about ± 0.2 Hz.

Figure 18 shows the resulting bifurcating phase diagram near the onset of instability for glycerin–water solutions at $\beta = 4.6°$. We use frequency instead of wavenumber as a parameter because the former is experimentally controlled. The following features are shown. (*a*) The circles are measurements of the *neutral stability curve* $f_c(R)$, and the upper solid line is the corresponding fit to the data. (This is similar to figure 4, but for

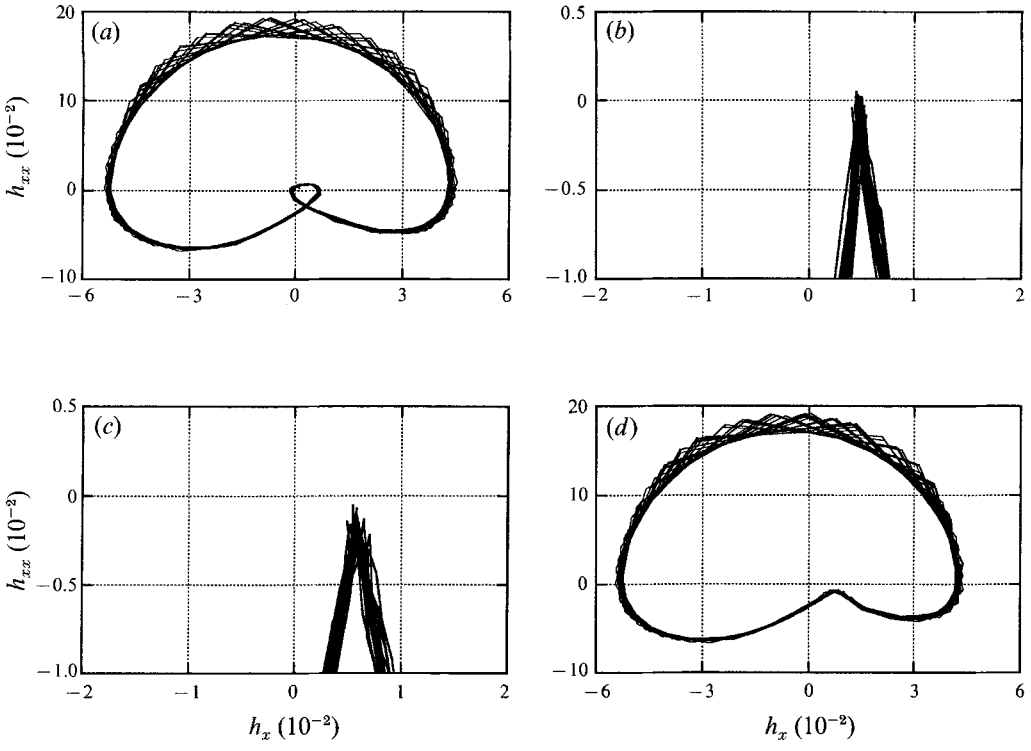

FIGURE 17. Determination of the phase boundary f_s^* (glycerin–water solutions, $\beta = 4.6°$, $R = 24.3$). The phase orbit in the (h_x, h_{xx})-plane changes with forcing frequency f: (*a*) $f = 3.4$ Hz; (*b*) $f = 4.1$ Hz, magnified view near the cusp; (*c*) $f = 4.2$ Hz, magnified view; (*d*) $f = 4.9$ Hz. The boundary f_s^* (where the extra zero crossings of h_{xx} are lost) is determined to be 4.2 Hz.

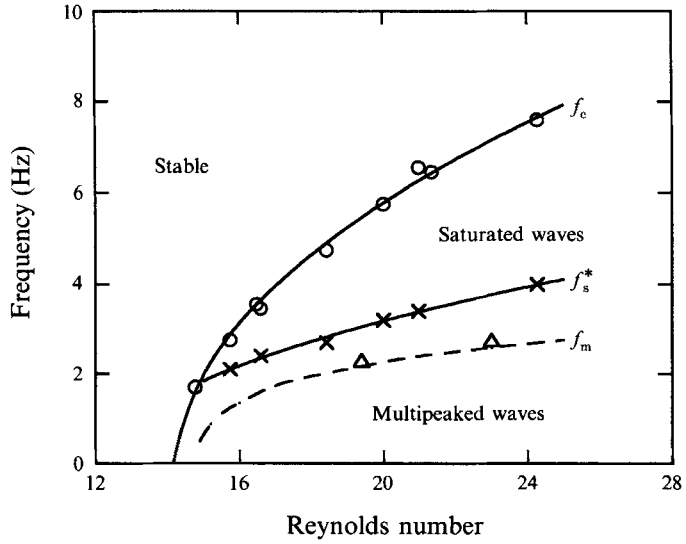

FIGURE 18. Linear and nonlinear phase diagram (glycerin–water solutions at $\beta = 4.6°$): Measurements of $f_c(R)$ and a fit to the data (○); the measured phase boundary $f_s^*(R)$ with a smooth line drawn through the data (×); the measured most rapidly amplified frequency $f_m(R)$ for linear waves (△), with predictions (----) from linear theory based on the method due to Anshus & Goren (1966).

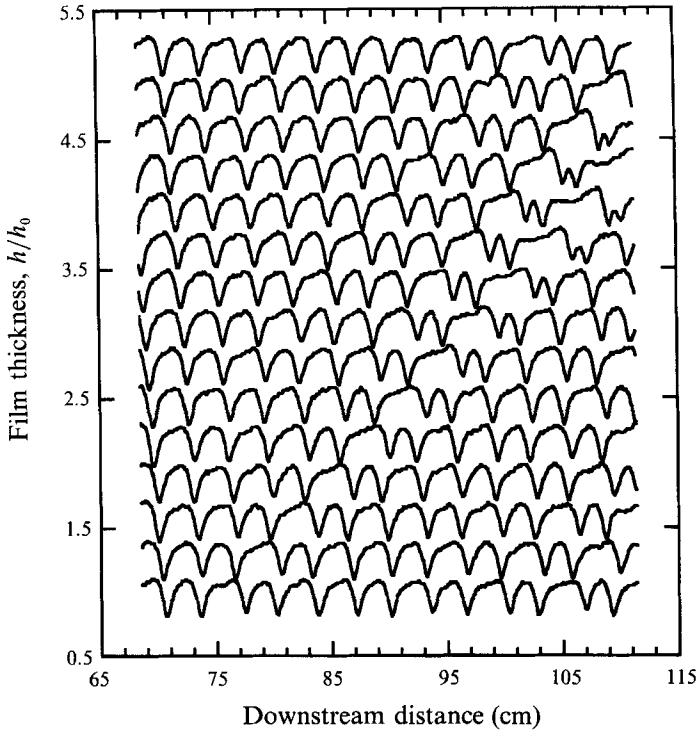

FIGURE 19. Spatial subharmonic instability of two-dimensional periodic waves (glycerin–water films, $\beta = 6.4°$, $R = 30$ and $f = 7$ Hz): spatiotemporal evolution of the film thickness h/h_0 at times separated by $\frac{2}{15}$ s. Wave profiles are displaced vertically from each other by 0.3.

a different angle.) (*b*) The crosses show the measured *phase boundary* $f_s^*(R)$, with a smooth line drawn through the data. (*c*) The triangles show measurements of the *maximum amplified frequency* $f_m(R)$, and the dashed line is $f_m(R)$ calculated from linear theory with the method due to Anshus & Goren (1966), but for the conditions of our experiment, with no adjustable parameters.

Between $f_c(R)$ and $f_s^*(R)$ in figure 18 we find saturated finite-amplitude waves with one maximum per period. Below $f_s^*(R)$, waves evolve into multipeaked waveforms. The initial stages of this process can be considered to result from the fact that in this regime the first several harmonics of the basic wave are unstable; they grow fast and lead to complicated modal interactions (Lin & Wang 1985; Joo & Davis 1992*a*). There is no quantitative theory for the nonlinear stages of this process. The phase boundary $f_s^*(R)$ increases with R, but it appears to intersect $f_c(R)$ instead of going to zero as R decreases to R_c. However, it is difficult to be confident about this intersection due to measurement limitations. It is interesting to note that the maximum amplified frequency $f_m(R)$ predicted by linear theory lies in the multipeaked (strong nonlinear) region. This is probably one reason for the fact that saturated periodic waves do not appear for natural (unforced) waves. Some simulations relevant to our observations have been made by Joo *et al.* (1991).

4.7. *Subharmonic instability of two-dimensional periodic waves*

It is important to study the secondary instability of two-dimensional periodic waves in order to understand the transitions to disordered flows. In this section, we briefly show that one secondary instability of two-dimensional periodic waves is a spatial

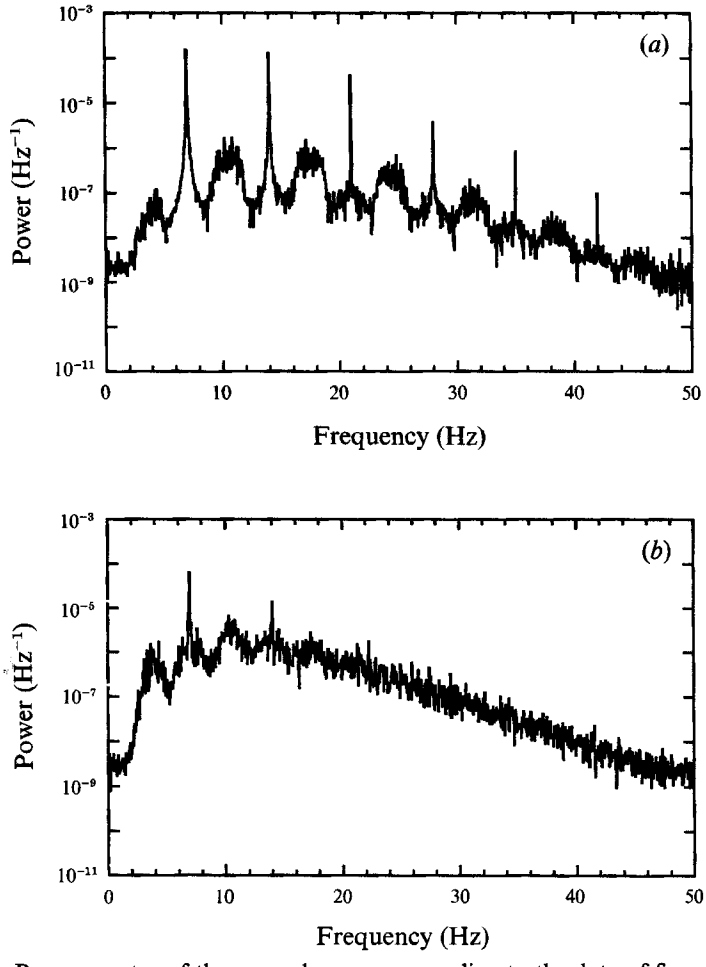

FIGURE 20. Power spectra of the wave slope corresponding to the data of figure 19 at (*a*) $x = 77$ cm and (*b*) $x = 108$ cm. The subharmonic character of the instability of periodic waves is evident.

subharmonic instability leading to more complex two-dimensional waves, and that it is convective as is the primary instability.

We find that periodic waves are unstable over a wide frequency band with respect to this subharmonic instability. An example is given in figure 19, which shows the spatiotemporal evolution of the film thickness in a section 43 cm long in the streamwise direction. Periodic waves with frequency $f_0 = 7$ Hz are initially generated near the source and are found to saturate roughly at $x = 50$ cm. Slight modulation of wavelength is visible at $x = 70$ cm and is amplified downstream. When a local wave spacing increases, the adjacent spacing decreases. Eventually, the waves coalesce in pairs, and therefore the period is roughly doubled.

We also studied this process using temporal spectra of local slope measurements, as shown in figure 20. These measurements show that broad spectral peaks appear at $f = (n+\frac{1}{2})f_0$, where n is an integer. This behaviour is consistent with the apparent spatial period doubling. However the period doubling is irregular both in space and in time because the subharmonic instability is convective and therefore sensitive to amplified noise. The irregular character of the process is evident spatially in figure 19, and is also apparent from the width of the spectral peaks in figure 20. It appears that

the subharmonic spectral peaks do not become dominant, and successive period-doubling processes do not exist. However, the irregularity generated by the instability of the periodic waves leads to spatiotemporal chaos farther downstream.

5. Discussion and conclusion

The main results of this investigation are as follows:

(i) The critical Reynolds number has been measured carefully as a function of angle (figure 5). (We have described in §4.1 the unusual experimental difficulties arising from the fact that the instability occurs at wavenumber $\alpha = 0$ at R_c.) The results are in excellent agreement with linear stability predictions. The growth rates and wave velocities have been measured carefully as functions of wavenumber (figure 14). They are also in good agreement with linear theory, though the computed wave velocities are a few percent below the measurements. This agreement implies that the approximations generally made in the linear stability theory of film flows are acceptable.

(ii) Fluorescence imaging provides an accurate way to measure the film thickness $h(x, y, t)$ in real time (figure 15), with a sensitivity of 3–4 μm. For two-dimensional waves, we are able to measure the local wave slope $s(x_0, t)$ by laser beam deflection with sensitivity of 5×10^{-5} (corresponding typically to wave amplitudes of 0.4 μm). This sensitivity is essential for understanding the role of input noise.

(iii) The initial instability has been demonstrated to be a convective one leading to noise-sustained patterns (for example, figure 2*c*). Film flows are very sensitive to external perturbations and are easily driven by a small periodic signal. External noise (or perturbations) initiates and sustains waves on the fluid interface. However, with increasing distance from the source, intrinsic nonlinearity gradually dominates the wave evolution, so that the waves become statistically independent of the input noise. The precise role of noise in the process of nonlinear evolution needs further study.

(iv) The nonlinear development of forced periodic waves depends strongly on the frequency. At low frequencies, the waves do not saturate, but instead generate subsidiary wavefronts (figure 15*a*). At higher frequencies, saturated finite-amplitude waves (figure 15*d*) are produced sufficiently far downstream. We measured the phase boundary $f_s^*(R)$ that separates these two types of bifurcation (figure 18). For unforced waves, the most rapidly growing frequency is too low to be in the saturated regime; this leads to subsidiary wavefronts that contribute to the irregular character of natural waves.

(v) Spatial subharmonic instability transforms periodic waves into disordered structures (figure 19). Periodic waves are unstable over a wide frequency band with respect to a subharmonic instability. Since this period-doubling instability is convective, its sensitivity to noise results in spatially varying wavelengths that are further amplified downstream.

Because of the difficulty of describing film flows quantitatively with the full hydrodynamic equations, long-wavelength evolution equations such as (5) have been proposed for studies of film flows. However, they can give incorrect results even for linear phenomena if R is too high. For example, (5) predicts a regime of absolute instability that is not found in experiments conducted at $R > 10$. However, some of the nonlinear phenomena exhibited by the long-wavelength evolution equations for low R persist at higher R, such as the existence of the phase boundary $f_s^*(R)$.

There are a number of issues not treated here that remain to be addressed in future work. First, the secondary instability of two-dimensional periodic waves has only been described to a limited extent here. Second, we have considered mainly two-dimensional

waves. There are several distinct mechanisms leading to three-dimensionality for different ranges of forcing frequency (Joo & Davis 1992; Liu *et al.* 1992). We intend to report in detail on various types of secondary instabilities in future publications. Finally, the statistical character of the regime of fully three-dimensional nonlinear waves remains to be explored.

We appreciate several helpful discussions with R. E. Kelly, S. H. Davis, S. W. Joo, and R. J. Deissler. E. Banilower participated in preliminary work. We also thank B. Gluckman, D. Vallette and T. Davis for assistance. The work was supported by the National Science Foundation under Grant CTS-9115005 (since early 1992) and by NSF Grant DMR-8901869 in 1991.

Note added in proof: In subsequent experiments (Liu & Gollub 1993) on the breakdown of two-dimensional periodic waves, we found that the character of the secondary instability is frequency-dependent. The subharmonic instability described in §4.7 predominates at low frequencies, and a sideband mechanism is more prominent close to the linear stability boundary of figure 18.

REFERENCES

AGRAWAL, S. K. & LIN, S. P. 1975 Nonlinear spatial instability of a film coating on a plate. *Trans. ASME* E: *J. Appl. Mech.* **42**, 580–583.

ALEKSEENKO, S. V., NAKORYAKOV, V. Y. & POKUSAEV, B. G. 1985 Wave formation on a vertical falling liquid film. *AIChE J.* **31**, 1446–1460.

ANSHUS, B. E. & GOREN, S. L. 1966 A method of getting approximate solutions to the Orr–Sommerfeld equation for flow on a vertical wall. *AIChE J.* **12**, 1004–1008.

BABCOCK, K. L., AHLERS, G. & CANNELL, D. S. 1991 Noise-sustained structure in Taylor–Couette flow with through-flow. *Phys. Rev. Lett.* **67**, 3388–3391.

BABCOCK, K. L., CANNELL, D. S. & AHLERS, G. 1992 Stability and noise in Taylor–Couette flow with through-flow. Preprint.

BENJAMIN, T. B. 1957 Wave formation in laminar flow down an inclined plane. *J. Fluid Mech.* **2**, 554–574.

BENJAMIN, T. B. 1961 The development of three-dimensional disturbances in an unstable film of liquid flowing down an inclined plane. *J. Fluid Mech.* **10**, 401–419.

BENNEY, D. J. 1966 Long waves on liquid films. *J. Math. Phys.* **45**, 150–155.

BERTSCHY, J. R., CHIN, R. W. & ABERNATHY, F. H. 1983 High-strain-rate free-surface boundary-layer flows. *J. Fluid Mech.* **126**, 443–461.

BRAUNER, N. & MARON, D. M. 1982 Characteristics of inclined thin films, waviness and the associated mass transfer. *Intl J. Heat Mass Transfer* **25**, 99–110.

CHANG, H.-C. 1989 Onset of nonlinear waves on falling films. *Phys. Fluids* A **1**, 1314–1327.

CHANG, H.-C., DEMEKHIN, E. A. & KOPELEVICH, D. I. 1993 Nonlinear evolution of waves on a falling film. *J. Fluid Mech.* (in press).

CHENG, M. & CHANG, H.-C. 1992 Subharmonic instabilities of finite-amplitude monochromatic waves. *Phys. Fluids* A **4**, 505–523.

CHIN, R. W., ABERHATHY, F. F. & BERTSCHY, J. R. 1986 Gravity and shear wave stability of free surface flows. Part 1. Numerical calculations. *J. Fluid Mech.* **168**, 501–513.

CHU, K. J. & DUKLER, A. E. 1974 Statistical characteristics of thin wavy films, Part II: Studies of the substrate and its wave structure. *AIChE J.* **20**, 695–706.

CHU, K. J. & DUKLER, A. E. 1975 Statistical characteristics of thin wavy films, Part III: Structure of the large waves and their resistance to gas flow. *AIChE J.* **21**, 583–595.

DEISSLER, R. J. 1987*a* Spatially growing waves, intermittency, and convective chaos in an open flow system. *Physica* D **25**, 233–260.

DEISSLER, R. J. 1987*b* The convective nature of instability in plane Poiseuille flow. *Phys. Fluids* **30**, 2303–2305.

DEISSLER, R. J. 1989 External noise and the origin and dynamics of structure in convective unstable systems. *J. Statist. Phys.* **54**, 1459–1488.

DEISSLER, R. J., ORON, A. & LEE, Y. C. 1991 Evolution of two-dimensional waves in externally perturbed flow on a vertical cylinder. *Phys. Rev.* A **43**, 4558–4561.

DEISSLER, R. J. & TO, W.-M. 1992 Noise-sustained structure in the Navier–Stokes equations: Taylor–Couette flow with through-flow. Preprint.

DUKLER, A. E. 1972 Characterization, effects and modeling of the wavy gas–liquid interface. In *Progress in Heat and Mass Transfer* (ed. G. Hetsroni, S. Sideman & J. P. Hartnet), vol. 6, pp. 207–234. Pergamon.

FULFORD, G. D. 1964 The flow of liquids in thin films. *Adv. Chem. Engng* **5**, 151–236.

GJEVIK, B. 1970 Occurrence of finite-amplitude surface waves on falling liquid films. *Phys. Fluids* **13**, 1918–1925.

GJEVIK, B. 1971 Spatially varying finite-amplitude wave trains on falling liquid films. *Acta Polytech. Scand.* Me 61, 1–16.

GOUSSIS, D. A. & KELLY, R. E. 1991 Surface wave and thermocapillary instabilities in a liquid film flow. *J. Fluid Mech.* **223**, 25–45.

HUERRE, P. & MONKEWITZ, P. A. 1990 Local and global instabilities in spatially developing flows. *Ann. Rev. Fluid Mech.* **22**, 473–537.

JOO, S. W. & DAVIS, S. H. 1992*a* Instabilities of three-dimensional viscous falling films. *J. Fluid Mech.* **242**, 529–547.

JOO, S. W. & DAVIS, S. H. 1992*b* Irregular waves on viscous falling films. *Chem. Engng Commun.* **118**, 111–123.

JOO, S. W., DAVIS, S. H. & BANKOFF, S. G. 1991 Long-wave instabilities of heated falling films: two-dimensional theory of uniform layers. *J. Fluid Mech.* **230**, 117–146.

KAPITZA, P. L. 1948 Wave flow of thin layers of a viscous fluid: I. The free flow. *Zh. Exp. Teor. Fiz.* **18**, 3. Also in *Collected Papers of P. L. Kapitza* (ed. D. Ter Haar), vol. 2, pp. 662–679. Pergamon, 1965.

KAPITZA, P. L. & KAPITZA, S. P. 1949 Wave flow of thin layers of a viscous fluid: III. Experimental study of undulatory flow conditions. *Zh. Exp. Teor. Fiz.* **19**, 105. Also in *Collected Papers of P. L. Kapitza* (ed. D. Ter Haar), vol. 2, pp. 690–709. Pergamon, 1965.

KELLY, R. E., GOUSSIS, D. A., LIN, S. P. & HSU, F. K. 1989 The mechanism for surface wave instability in film flow down an inclined plane. *Phys. Fluids* A **1**, 819–828.

KOEHLER, R. 1968 Dissertation, Georg-August-Universität, Gottingen.

KRANTZ, W. B. & GOREN, S. L. 1970 Finite-amplitude, long waves on liquid films flowing down a plane. *Ind. Engng Chem. Fundam.* **9**, 107–113.

KRANTZ, W. B. & GOREN, S. L. 1971*a* Stability of thin liquid films flowing down a plane. *Ind. Engng Chem. Fundam.* **10**, 91–101.

KRANTZ, W. B. & GOREN, S. L. 1971*b* Bimodal wave formation on thin liquid films flowing down a plane. *AIChE J.* **17**, 494–496.

KRANTZ, W. B. & OWENS, W. B. 1973 Spatial formulation of the Orr–Sommerfeld equation for thin liquid films flowing down a plane. *AIChE J.* **19**, 1163–1169.

LACY, C. E., SHEINTUCH, M. & DUKLER, A. E. 1991 Methods of deterministic chaos applied to the flow of thin wavy films. *AIChE J.* **37**, 481–489.

LEE, J. 1969 Kapitza's method of film flow description. *Chem. Engng Sci.* **24**, 1309–1320.

LIN, S. P. 1969 Finite-amplitude stability of a parallel flow with a free surface. *J. Fluid Mech.* **36**, 113–126.

LIN, S. P. 1974 Finite amplitude side-band stability of a viscous film. *J. Fluid Mech.* **63**, 417–429.

LIN, S. P. & WANG, C. Y. 1985 Modeling wavy film flows. in *Encyclopedia of Fluid Mechanics* (ed. N. P. Cheremisinoff), vol. 1, pp. 931–951. Gulf.

LIU, J. & GOLLUB, J. P. 1993 Onset of spatially chaotic waves on flowing films. *Phys. Rev. Lett.* (submitted).

LIU, J., PAUL, J. D., BANILOWER, E. & GOLLUB, J. P. 1992 Film flow instabilities and spatiotemporal

dynamics. In *Proc. First Experimental Chaos Conf.* (ed. S. Vohra, M. Spano, M. Shlesinger, L. M. Pecora & W. Ditto), pp. 225–239. World Scientific.

NAKAYA, C. 1975 Long waves on a thin fluid layer flowing down an inclined plane. *Phys. Fluids* **18**, 1407–1420.

NAKAYA, C. 1989 Waves on a viscous fluid film down a vertical wall. *Phys. Fluids* A **1**, 1143–1154.

PIERSON, F. W. & WHITAKER, S. 1977 Some theoretical and experimental observations of the wave structure of falling liquid films. *Ind. Engng Chem. Fundam.* **16**, 401–408.

PROKOPIOU, T., CHENG, M. & CHANG, H.-C. 1991 Long waves on inclined films at high Reynolds number. *J. Fluid Mech.* **222**, 665–691.

PUMIR, A., MANNEVILLE, P. & POMEAU, Y. 1983 On solitary waves running down an inclined plane. *J. Fluid Mech.* **135**, 27–50.

ROSKES, G. J. 1970 Three dimensional long waves on a liquid film. *Phys. Fluids* **13**, 1440–1445.

SCHATZ, M. F., TAGG, R. P. & SWINNEY, H. L. 1991 Supercritical transition in plane channel flow with spatially periodic perturbations. *Phys. Rev. Lett.* **66**, 1579–1582.

SHKADOV, V. Y. 1967 Wave flow regimes of a thin layer of viscous fluid subject to gravity. *Izv. Akad. Nauk. SSSR, Mekh. Zhid. Gaza*, No. 1, 43–51. (English translation: *Fluid Dyn.* **2**, 29–34.)

SIVASHINSKY, G. I. & MICHELSON, D. M. 1980 On irregular wavy flow of a liquid film down a vertical plane. *Prog. Theor. Phys.* **63**, 2112–2114.

STEINBERG, V. & TSAMERET, A. 1991 Noise-modulated propagating pattern in a convectively unstable system. *Phys. Rev. Lett.* **67**, 3392–3395.

TAILBY, S. R. & PORTALSKI, S. 1962 The determination of the wavelength on a vertical film of liquid flowing down a hydrodynamically smooth plate. *Trans. Inst. Chem. Engrs* **40**, 114–122.

TRIFONOV, Y. Y. 1992 Steady-state traveling waves on the surface of a viscous liquid film falling down on vertical wires and tubes. *AIChE J.* **38**, 821–834.

TRIFONOV, Y. Y. & TSVELODUB, O. Y. 1991 Nonlinear waves on the surface of a falling liquid film. Part 1. Waves of the first family and their stability. *J. Fluid Mech.* **229**, 531–554.

TSVELODUB, O. Y. 1980 Stationary travelling waves on a film falling down an inclined plane. *Izv. Akad. Nauk. SSSR, Mekh. Zhid. Gaza*, No. 4, 142–146. (English translation: *Fluid Dyn.* **15**, 591–594.)

WHITAKER, S. 1964 Effect of surface active agents on stability of falling liquid films. *Ind. Engng Chem. Fundam.* **3**, 132–142.

YIH, C. S. 1955 Stability of parallel laminar flow with a free surface. In *Proc. 2nd US Congr. on Applied Mechanics*, pp. 623–628. ASME.

YIH, C. S. 1963 Stability of liquid flow down an inclined plane. *Phys. Fluids* **6**, 321–330.